Title

Epitaxial Transition Metal Dichalcogenide Films on GaN: Growth in High Vacuum and Characterization

Author

Yang, Hae In

Publication Date

2024

UNIVERSITY OF CALIFORNIA
RIVERSIDE

Epitaxial Transition Metal Dichalcogenide Films on GaN: Growth in High Vacuum and Characterization

A Dissertation submitted in partial satisfaction
of the requirements for the degree of

Doctor of Philosophy

in

Materials Science and Engineering

by

Hae In Yang

June 2024

Dissertation Committee:
Dr. Ludwig Bartels, Chairperson
Dr. Mahesh Neupane
Dr. Shane Cybart

The Dissertation of Hae In Yang is approved:

Committee Chairperson

University of California, Riverside

Acknowledgements

I would like to express my thanks to those whom I owe gratitude in this academic journey as a graduate student at UCR.

Above all, I am deeply indebted to my supervisor, Prof. Ludwig Bartels. I feel privileged to have learned in depth and gained much knowledge under his guidance and support. My understanding would not have deepened, and my work would not have been advanced without his knowledge, guidance, and inspiration. I also thank Profs. Cengiz Ozkan, Elaine Haberer, Peter Alexander Greaney, Reza Abbaschian, Jianlin Liu, and Yadong Yin. Through their lectures, I could solidify my understanding of material science. I am grateful to Profs. Mahesh Neupane and Shane Cybart, for serving on my doctoral dissertation committees.

I greatly appreciate my mentor, Dr. Kortney Almeida, who has been much more than a research mentor to me. Her wisdom from experience and encouragement helped me to move on during the difficult periods. It also has been a pleasure working with senior, fellow students and friends: Dr. Michelle Wurch, Daniel Coyle, Prachi Yadav, Jing Jin, Bryan Flores, Nicolas Meneses, Ricardo Dacosta, Abinaya Sushana, Martin Juarez, Meagan Hill, and Sandra Villarreal, especially Yuying for her strong work ethic and unwavering support. I learned techniques and insights from them, and I am thankful for their support and enjoyable discussions in all aspects.

I would like to thank Prof. Woong Choi at Kookmin University. Being in the US would not be imaginable without his support and encouragement. I owe thanks to my old friends in Korea for their understanding and consideration.

The continuous love and encouragement from my parents and brother keep me motivated and going through challenging moments. Also, many thanks to Pam and my yoga teacher, Yvonne for their support. Their encouragement inspires me to improve myself.

Abstract of the Dissertation

Epitaxial Transition Metal Dichalcogenide Films on GaN:
Growth in High Vacuum and Characterization

by

Hae In Yang

Doctor of Philosophy, Graduate Program in Materials Science and Engineering
University of California, Riverside, June 2024
Dr. Ludwig Bartels, Chairperson

2D materials such as Transition metal dichalcogenides (TMDs), MoS_2 and WS_2, possess unique properties, namely tunable bandgap, novel optical and electronic characteristics, generating substantial interest as promising materials for transistors and photodetectors. 2D materials incorporated with 3D material can enhance device performance by the interfacial and epitaxial relationship between 2D materials and 3D materials such as Gallium Nitride (III–V semiconductors), which is almost perfectly lattice matched with MoS_2. Although several studies have explored an understanding of the interface and device performance of 2D/3D material integration, we offer in-depth insight into the optimization of the interface and a unique growth process for integrating TMDs and GaN under a high vacuum system ($\sim 10^{-7}$ torr). Therefore, the aim of this dissertation research is to discuss an epitaxial growth mechanism and characteristics of heterostructures.

The first part of the dissertation research aimed to optimize the in-situ interface preparation of GaN by Neon sputtering and ammonia annealing treatment before growing MoS_2 in a high vacuum system. We achieved epitaxial growth of MoS_2 on nitrogen-terminated GaN surface, resulting in 2 × 2 reconstruction acquired by low-energy electron diffraction (LEED). The MoS_2/GaN diode exhibited a high on-off ratio of $\sim 10^5$ at 1 V and a low turn-on voltage (~0.3 V), resembling a Schottky diode.

The second part of the project attempted optimization of in situ epitaxial growth of GaN on MoS_2 without MoS_2 removed. GaN growth was controlled by substrate temperature, Gallium evaporation rate and high voltage for filaments to activate ammonia. The structural quality of the GaN/MoS_2 films was evaluated through X-ray photoelectron spectroscopy (XPS) and Raman spectroscopy.

In the third part, bright photoluminescence (PL) in TMD heterostacks, alternating layers of MoS_2 and WS_2 on GaN, was explored. Layer by layer and 3R (Rhombohedral) type stacking TMD films were confirmed by Cross-sectional transmission electron microscopy (TEM). In electrical transport characteristics, The TMDs heterostacks show a Schottky-diode behavior with a high on-off ratio of up to 10^6 and the breakdown voltage under -100V. Furthermore, the comparison of wafer scale WS_2/MoS_2 vs MoS_2/WS_2 is investigated.

Table of Contents

List of Publications

Yang, H. I.; Ning,Y.; Jin,J.; Juarez, M.; Henshaw, J.; Azizur-Rahman, K.; Flores, B.; Meneses, N.; Yadav, P. R.; Villarreal, S; Hill, M. E.; Sorger, V.; Mounce, A.; and Bartels, L., Photoluminescent Substrate-Scale 3R WS_2/MoS_2 Heterostacks on GaN. (in review)

Yang, H. I.; Coyle, D. J.; Wurch, M.; Yadav, P. R.; Valentin, M. D.; Neupane, M. R.; Almeida, K.; Bartels, L., Epitaxial Molybdenum Disulfide/Gallium Nitride Junctions: Low-Knee-Voltage Schottky-Diode Behavior at Optimized Interfaces. ACS Applied Materials & Interfaces **2021**, 13 (29), 35105–35112.

List of Figures

Chapter 1: Introduction

Chapter 2: Instrumentation

Chapter 3: Epitaxial MoS_2/GaN diode with a low knee voltage

Chapter 4: Growth of GaN on MoS_2

Chapter 5: WS_2/MoS_2 Vertical Heterostacks on GaN

Chapter 1: Introduction

1.1 2D materials: Transition Metal Dichalcogenides

The existence of bandgaps in transition metal dichalcogenides (TMDs) (e.g., MoS_2, WS_2, $MoTe_2$) offers an attractive possibility of using these layered materials in various device applications.[1] Single-layer TMDs with direct bandgaps are promising for optoelectronic applications since the band structure of TMDs depends on their thickness.[2] MoS_2 is a typical example of TMDs and has been most researched. The single layer or few layers of MoS_2 thin film transistors have been studied to perform a high on/off ratio($\sim 10^8$) and mobility of > 200 cm^2/Vs.[3] Ultrathin TMDs have been made to utilize chemical vapor deposition (CVD),[4] metal–organic CVD (MOCVD),[5] and atomic layer deposition (ALD).[6] Owing to weak Vander Waals interaction between layers, thin TMDs can be easily exfoliated from their bulk forms.[7] TMDs like MoS_2 and WS_2 can exist in several phases: 2H, 1T, and 3R. 2H-MoS_2 is the most thermodynamically stable arrangement, as shown in Fig. 1.1, and 3R-MoS_2 is the second most stable phase of MoS_2.[8]

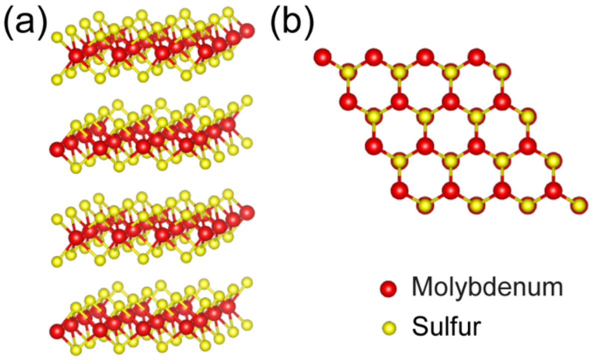

Figure 1.1 (a) Side view (b) top view of an atomic representation of 2H-MoS_2

1.2 3D materials: Gallium Nitride

Gallium nitride (GaN) has been one of the most promising materials for use in wide bandgap semiconductors with electronics and optoelectronic devices over the past years.[9] Gallium nitride, initially introduced into semiconductor technology as a wide-band-gap (~3.4 eV) material able to provide blue light-emitting diodes[10] has found a number of additional applications for power conversion.[11] However, the lack of a lattice-matched and thermally compatible substrate to GaN is a major challenge. Also, large-area deposition, the crystallinity of the grown layers, and the residual stress are important general issues in the epitaxial growth or the deposition of the functional layers. Nucleation difficulties at high temperatures and mismatching of a lattice are typically observed during the growth of GaN directly on a substrate. For those reasons, most GaN films are grown on thin buffer layers of either A1N or AlGaN. Most of the GaN films grown have a hexagonal wurtzite crystal structure, which is characterized by the lattice parameters a_0 (3.189 Å) and c_0 (5.185 Å).[12] Molecular beam epitaxy (MBE) and Metalorganic chemical vapor deposition (MOCVD) are the most common techniques for GaN growth.

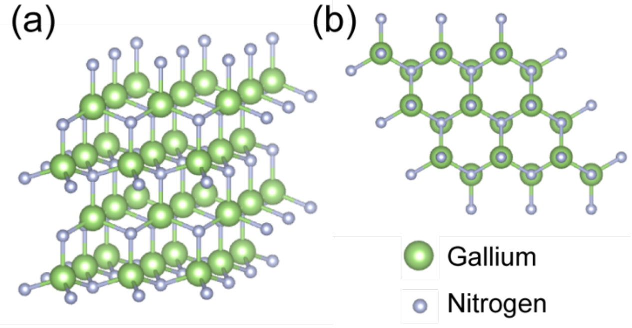

Figure 1.2 (a) Side view (b) top view of atomic representation of GaN

1.3 Epitaxial growth

Epitaxy comes from the Greek words: epi- means above/on top of, and -taxis means an ordered manner.[13] Epitaxial growth refers to a crystallographic-oriented growth between the crystalline substrate and vertically stacked film. There are two types of epitaxy, homoepitaxy and heteroepitaxy. Homoepitaxy is when a grown film matches the material of its substrate, while heteroepitaxy is when a grown film is a different material from its substrate.[13] In this dissertation research, we focused on heteroepitaxy between TMD materials and GaN. In heteroepitaxy, similar lattice parameters and crystallographic orient relationships between epilayers and substrate are required to achieve desired applications. The lattice parameters of 2D materials and 3D materials are summarized in Table 1.1.

Materials	Phase	a [Å]	Materials	Phase	a [Å]
MoS_2	2H	3.160 [14]	PtS_2	1T	3.591 [15]
$MoTe_2$	2H	3.519 [16]	$PtSe_2$	1T	3.785 [15]
	1T	3.493 [17]	$PtTe_2$	1T	4.069 [15]
	1T'	3.454 [17]	HfS_2	1T	3.635 [18]
$MoSe_2$	2H	3.288 [14]	$HfSe_2$	1T	3.748 [18]
WS_2	2H	3.153 [14]	GaN	2H	3.189 [19]
WTe_2	2H	3.600 [16]			
WSe_2	2H	3.260 [14]			

Table 1.1 Lattice parameters of TMDs and GaN

Epitaxial growth has been an important technique in heterostructure device applications with the integration of 2D and 3D materials. For instance, integration devices with GaN and MoS_2 have the potential to take advantage of conventional 3D semiconductors and the unique properties of thin 2D films. Furthermore, MoS_2 and GaN combination offers ideal epitaxial growth conditions since GaN and MoS_2 possess in-plane lattice mismatch of only ~0.8% and thermal expansion coefficient mismatch of 1%.[19]

Chapter 2: Instrumentation

2.1 High Vacuum Growth Chamber

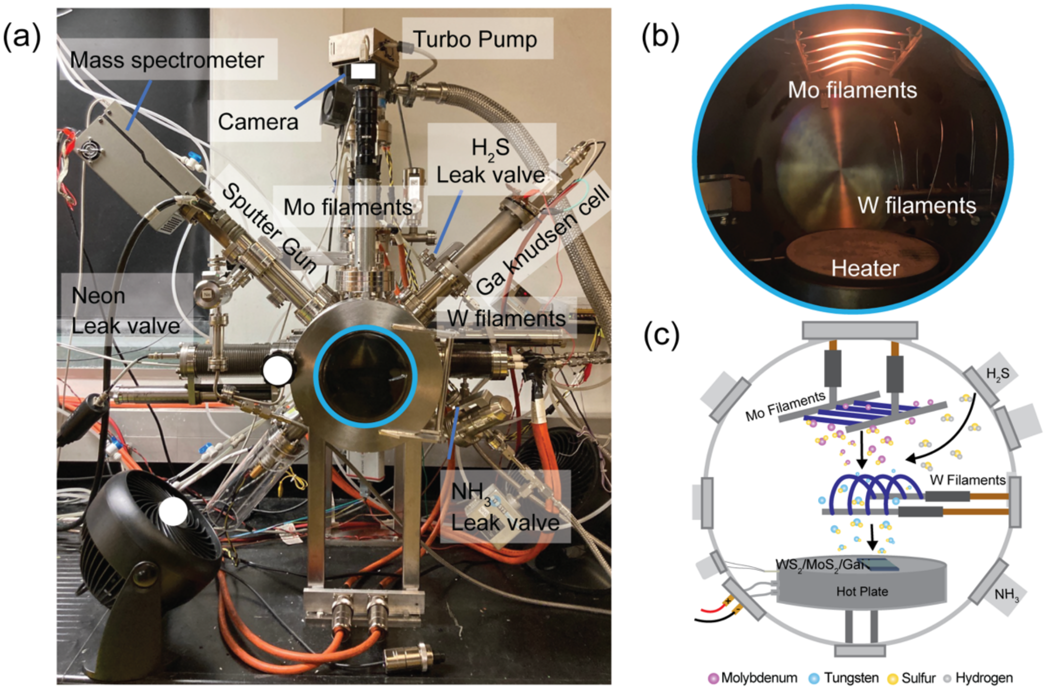

Figure 2.1 (a) Photo of the high vacuum growth chamber (b) Photo of the chamber inside during MoS_2 deposition (c) Schematic representation of the growth reactor.

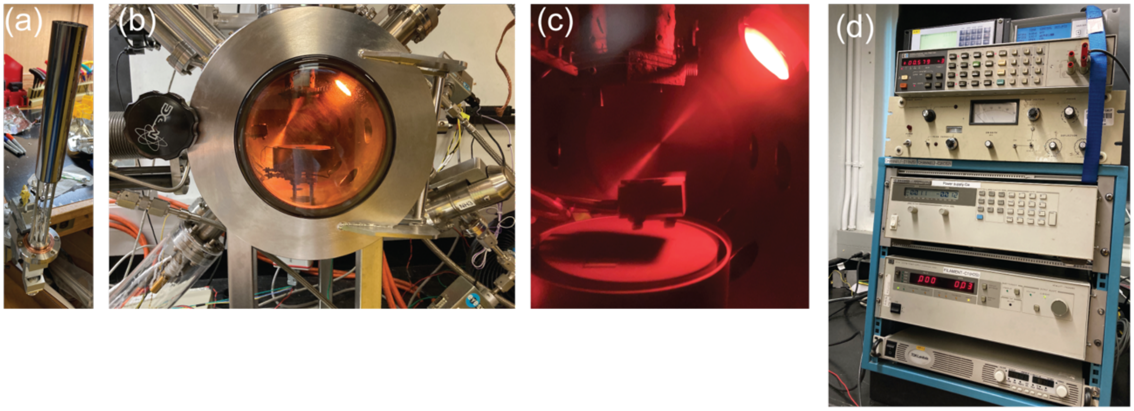

Figure 2.2 Photo of (a) the gallium Knudsen cell (b) the chamber during Gallium deposition (c) chamber inside (d) Thin film thickness monitor, power supply for Knudsen cell, multimeter for thermocouple.

A vacuum chamber is equipped with a rough pump and a turbo pump to achieve high vacuum at 10^{-7} torr. It sets up a leak valve for H_2S, NH_3, and Ne, as shown in Figure 2.1(a). In order for Ion sputtering on the blank substrate, the sputter gun is equipped with a leak valve, which allows neon gas to be leaked. A mass spectrometer is set up to find leaks in vacuum chambers using helium and detect the various gases from gas lines to approach a clean environment for growth. In figure 2.2 (a), a Knudsen cell filled with Gallium (Alfa, 99.9999%) is used to deposit gallium nitride films and is controlled remotely via a power supply (Agilent 6653A). In Figure 2.1(b), 2.2 (c) and (d), quartz crystal sensors on the left flange port equipped with a thin film thickness monitor are used to monitor evaporation rate and thickness, leading to a reliable process for GaN growth. A Video camera mounted on the top of the observation window is used to monitor colorimetric measurements of the reflection of the filaments from the sample. Inside the fast access entry door, a 3-inch hot plate and sets of 0.5mm Molybdenum of 0.5mm thickness and Tungsten filaments of 0.2794mm thickness are installed, as shown in Figure

2.1(b). The heater is controlled by a power supply (Agilent 6675A), and filament power is controlled via a switch relay box and power supply (Agilent 6031A) remotely through a LabVIEW program.

2.2 Ultra-High Vacuum techniques

Low energy electron diffraction and X-ray photoelectron spectroscopy need to be operated under ultra-high vacuum (~10^{-9} to 10^{-10} torr) since otherwise, the mean free path of electrons or ions would be too small, and the surface would be covered with contaminants from the residual atmosphere so that we wouldn't get any useful results. The ultra-high vacuum can be reached by turbomolecular pumps, which cannot be operated under the atmosphere, so rotary oil pumps are required to obtain a low vacuum (~10^{-2} torr) before pumping down turbo pumps. The gas inside the chamber and water on the wall are removed quickly by heating so that bake-out at a temperature over 100 °C is applied. To measure pressure in a range of 10^{-3} and 10^{-11} torr, we use ionization gauges.

2.3 Low Energy Electron Diffraction

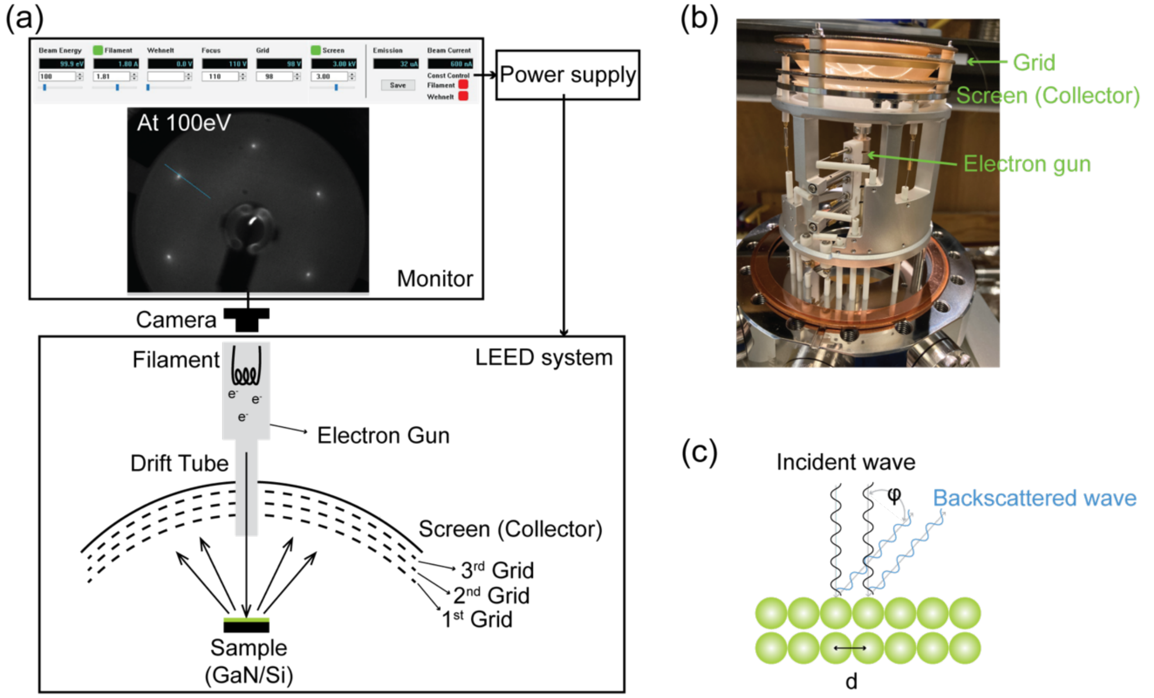

Figure 2.3 (a) Schematic of computer-controlled LEED system and the obtained LEED image of GaN at a beam energy of 100eV on the monitor (b) Photo of LEED system (upside down) (c) scattering of wave at a lattice.

Low energy electron diffraction (LEED) is the common technique to study the order of periodic surface structures and partially disordered structures. L. de Broglie proposed the concept of wave-like behavior of matter, and it follows de Broglie waves equation: $\text{Wave length}\ \lambda = \frac{h}{mv}$, $\text{Planck's constant}\ h, \text{velocity}\ v, and\ \text{mass}.$ As for electrons, the wavelength for 100 eV (low energy) electrons is 1.2 Å from the equation. Considering the universal curve[20], the mean free path of electrons at a range of 20 eV to 300 eV is below 1nm, indicating only electrons scattered from near the surface can be emitted, which means LEED is a surface-sensitive technique.

As shown in Fig 2.2 (a), electrons emitted from filaments leave and move through the drift tube of the electron gun with the desired energy and hit the GaN sample surface. Backscattered electrons from the surface pass toward three hemispherical grids. The first grid is grounded, leading the scattered electrons not to be deflected between the first grid and the sample. The second grid is biased negative potential, slightly smaller than electron energy, so that repels the inelastically scattered electrons. In this experiment, we used a grid, which is 2 eV less than electron energy. Elastically scattered elections pass 2nd grid and are accelerated onto a screen by kilovolts positive potential (3kV). The 3rd grid is used for the improvement of LEED patterns by avoiding field inhomogeneities.[15.] Our LEED system from OCI Vacuum Microengineering Inc (BDL 800IR) is built in an ultra-high vacuum chamber. It controls energy and filament current from the power supply remotely and observes diffraction patterns of hexagonal crystalline GaN substrate through a camera.

The principle of the diffraction pattern formation is started from Bragg's Law, as shown in Fig 2.2 (c). Once an incident wave of electrons scatters at a lattice spot, backscattered wave interference occurs given by the equation: $n\lambda = d\ sin\varphi$ (a is the distance between lattice spots, n is an order of diffraction, and φ is the angle between the incident and scattered).[21] This equation determines the direction of the scattered wave and diffraction spots on the screen. For example, GaN has a sharp hexagonal diffraction pattern (1×1) due to the periodicity of GaN (0001).

2.4 X-ray Photoelectron Spectroscopy

X-ray photoelectron spectroscopy (XPS) is a useful technique to obtain information on a surface to a depth 7-110 Å: a. Elements' identification in the surface, b. Quantitative analysis, c. Oxidation state, d. Charge transfer, e. Valence band edge below Fermi level.

Figure 2.3 shows an illustration of XPS system and acquired results. The principle of the X-ray source is that electrons from the filament are emitted by thermionic emission, and they are accelerated onto the anode at a high voltage (~ +14kV). The anode needs to be water-cooled since a lot of power is generated in the X-ray source. The anode is covered with metal, typically Aluminum (Al Kα=1486.6 eV) and Magnesium (Mg Kα 1253.6eV). X-rays are generated with energy depending on anode materials and leave the source through a thin Aluminum foil window. X-rays move toward a sample and penetrate a few nanometers of the sample surface and excite photoelectrons with kinetic energy. Photoelectrons with different kinetic energy can travel on the surface in the range of 1 and 100 Å depends on universal curve.[20] The ejected photoelectrons move to the analyzer and are energy segregated. The elections passed through slit travel depending on the potential difference (Pass energy, E_p) between the inner and the outer hemisphere. With a smaller pass energy, a higher energy resolution and less elections counted. When the electrons arrive at a detector, the electrons with higher kinetic energy travel close to outer hemisphere so that electrons are energy-segregated. A detector consists of two microchannel plates that amplify electron counts. Multiplied electrons that pass through plates head to phosphors screen, and we can observe electron counts correspond to a certain kinetic energy through a CCD camera. When Kinetic energy (E_k) converts to binding energy (E_b) with following equation: $E_b = h\upsilon - E_k - e\varphi$ ($h\upsilon$ photon energy and φ work function of spectrometer), an image with y-direction as a function of binding energy is produced. The counts in the image are integrated to collect plots with counts as function of binding energy. For our work, XPS was carried out using an X-ray source from PSP vacuum tech. TX400/2 and electron analyzers from Scienta omicron.

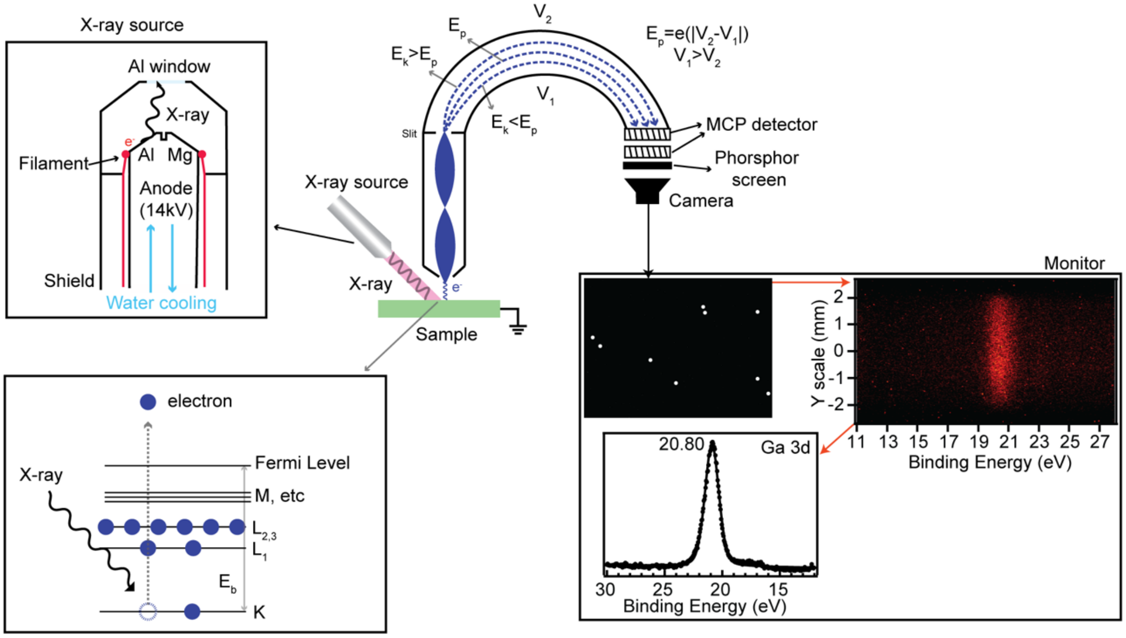

Figure 2.4 Illustration of XPS system and obtained results of GaN sample.

2.5 Photoluminescence

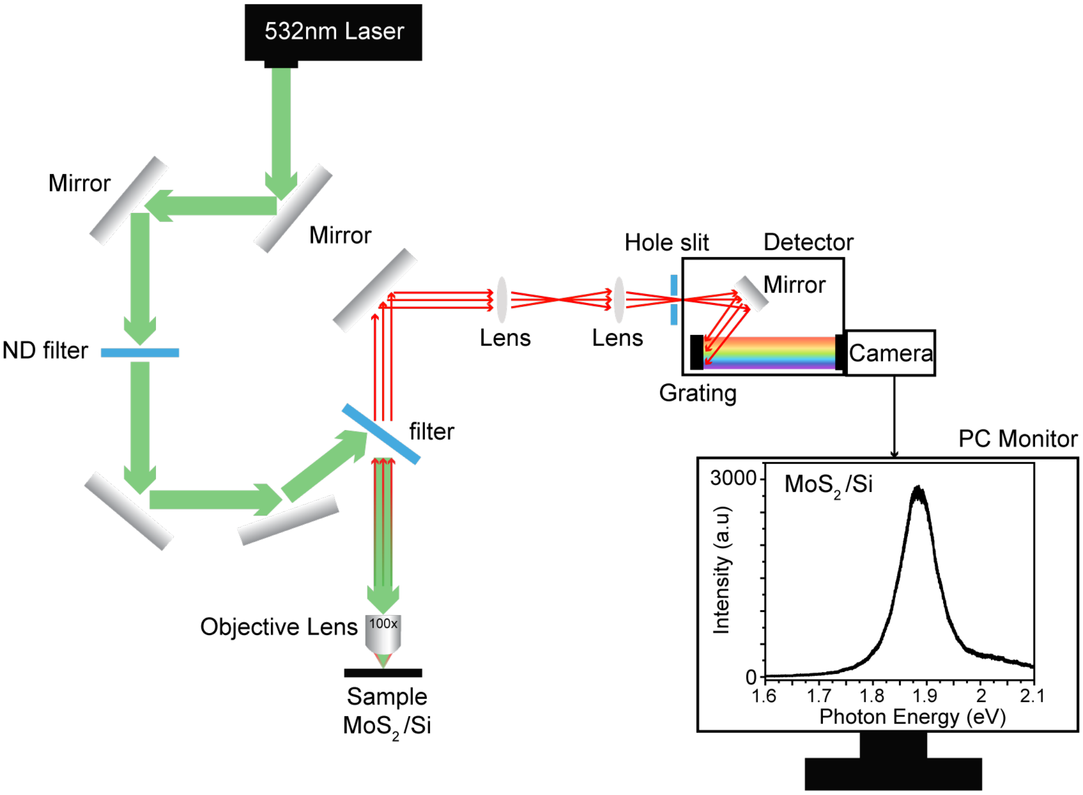

Figure 2.5 Schematic of PL/Raman system and observed PL peak at 1.9 eV of MoS$_2$/Si on the monitor

When TMD materials absorb the laser with 532 nm, which provides photons with energy larger than the band gap, the electrons in films are excited to the conduction band, and holes are created at the Valence band. In direct bandgap, excited electrons go back to the VB and emit energy, forming excitons, electron, and hole pairs, which are attracted to each other by coulomb force. Single layer MoS$_2$ and WS$_2$ have a direct bandgap, leading strong PL around 1.85 eV and 2.02 eV of Photon Energy, respectively. On the other hand, multilayer MoS$_2$ and WS$_2$ have indirect bandgap, showing low intensity and lower photon energy peak due to non-radiative recombination and smaller bandgap. Also, defects or oxidation of film causes the non-radiative recombination which leads reduction of PL intensity.[7] Multilayer WS_2/MoS_2 stacked films have a unique PL characteristics, described in further detail in the next chapter.

Our samples were analyzed with PL/Raman using a HORIBA LabRAM with a 532nm excitation laser. Figure 2.4 shows how the optics work. 532 nm laser reflected off by several mirrors passes through 100x objectives and hits the sample. Raman/ PL signal from the sample hit the filter to set apart backscattered laser light. The signal is focused through a hole slit and dispersed by the grating (1800 grooves/mm), which allows the signal to separate the constituent wavelength and scatter onto a CCD camera. Typically, there were 600 and 1800 grating and higher grating is used for better resolution, but fewer counts and a longer duration.

2.6 Device Fabrication

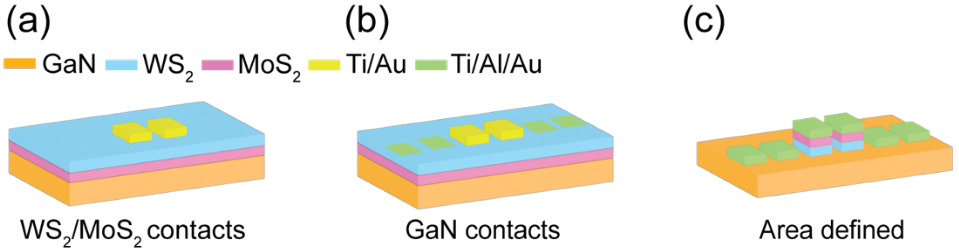

Figure 2.6 Schematic representation of $WS_2/MoS_2/GaN$ device fabrication (a) 1st patterning for WS_2/MoS_2 (b) 2nd pattenring for GaN contacts (c) 3rd patterning for area defined

To investigate transport characteristics of 2D materials on 3D materials, we patterned diodes using E-beam lithography (EBL) and E-beam evaporator. Fabrication consists of multiple steps: first, the substrate is spun down with a few hundred nm of

PMMA resist C5 and proceeded to bake at 150 °C for 90 s. MoS_2 contact areas(120um×120um) are defined by EBL system and then MIBK is used to develop the patterns. The sample is loaded in an E-beam evaporator system, and a 5 nm titanium/50 nm gold stack is deposited on the sample [Figure 2.5a]. After liftoff using Acetone and deposition of a new resist layer, the sample is loaded in an XPS chamber to remove MoS_2 films via sputtering with argon at 3 keV and define GaN. Without breaking the vacuum, a 5 nm of Ti and 50 nm of Al stack is deposited. After Al deposition, the sample is transferred through air to an evaporator in clean room and 50nm of gold as a capping layer is deposited [Figure 2.5b]. After liftoff, the third lithographic step begins by defining the area between the contacts and MoS_2 is removed by Ar sputtering at 3keV. The final device is shown in Figure 2.5c.

2.7 Transport characteristics

The transport characteristics are measured by a four-probe method in this research in order to exclude contact resistance and calculate the voltage drop across where we are interested (e.g., MoS_2/GaN stack). DC current from Keithley 2400 is operated between the source and drain contact pad through probe tips. Two electrometers read the voltage drop depending on where electrometers are applied. As shown in Figure 2.6a, the electrometer (V_{sense1}) reads a voltage drop in GaN contact resistance (R_{GaN}) and the electrometer (V_{sense2}) reads a voltage drop in GaN channel resistance (R_{ch}) and GaN contact resistance (R_{GaN}). When the Voltage source substrate V_{sense2}, only resistance in MoS_2, which we aim to calculate, remains. Therefore, we can approximate transport characteristics dominated by MoS_2 [Figure 2.6c].

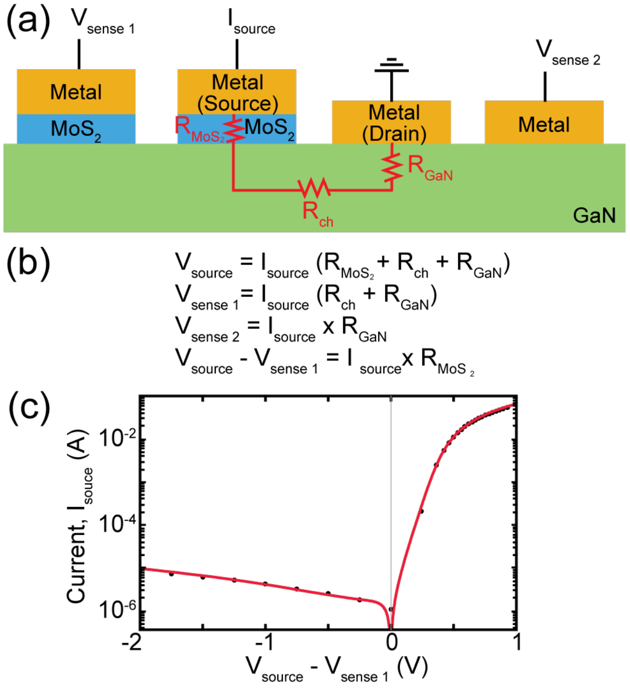

Figure 2.7 (a) Schematic of MoS_2/GaN diode with 4-probe terminal. (b) Relation of Voltage drop and Resistance. (c) logarithmic plot of Current-Voltage characteristics of MoS_2/GaN diode.

Chapter 3: Epitaxial MoS_2/GaN diode with a low knee voltage

The following chapter contains excerpts from “Epitaxial Molybdenum Disulfide/Gallium Nitride Junctions: Low-Knee-Voltage Schottky-Diode Behavior at Optimized Interfaces” by **Yang, H. I.**, Coyle, D. J., Wurch, M., Yadav, P. R., Valentin, M. D., Neupane, M. R., Almeida, K., and Bartels, L.

3.1 Motivation

MoS_2 and GaN are almost perfectly lattice-matched at a mismatch of only ~0.8%, while offering complementary properties in many respect including: MoS_2 is a layered material facile to grow by chemical vapor deposition (CVD) on a great number of substrates,[22] while GaN's lattice is nonlayered so that CVD growth requires well matched substrates for appreciable material properties[23]. Heterostructures application with epitaxial grown MoS_2 on GaN offer large untapped technological opportunities, their realization and utility rely on understanding of the material interface both for MoS_2 grown on GaN and, ultimately, the reverse.

Several prior studies addressed the growth of MoS_2 on GaN. Work at the Army Research Lab in collaboration with the Robinson group showed growth of MoS2 single- and multilayer islands as well as films aligned with the GaN substrate.[24] The absence of photoluminescence from these MoS_2 islands was noted. Extension to thicker layers by means of "metal-organic CVD (MOCVD)"[25] using carbonyl precursors in a flow reactor led to well-layered MoS_2 material separated by several disordered substrates/interfacial layers from the GaN substrate.

The presence of van der Waals (vdW) gaps above and below each MoS_2 layer reduces its interaction with GaN and facilitates its layered crystalline growth, but it also reduces the propensity of such growth for epitaxy. Here, we offer detailed insight into the optimization of the former interface using a broad range of surface science and ex situ techniques.

3.2 Optimization of MoS_2/GaN interface

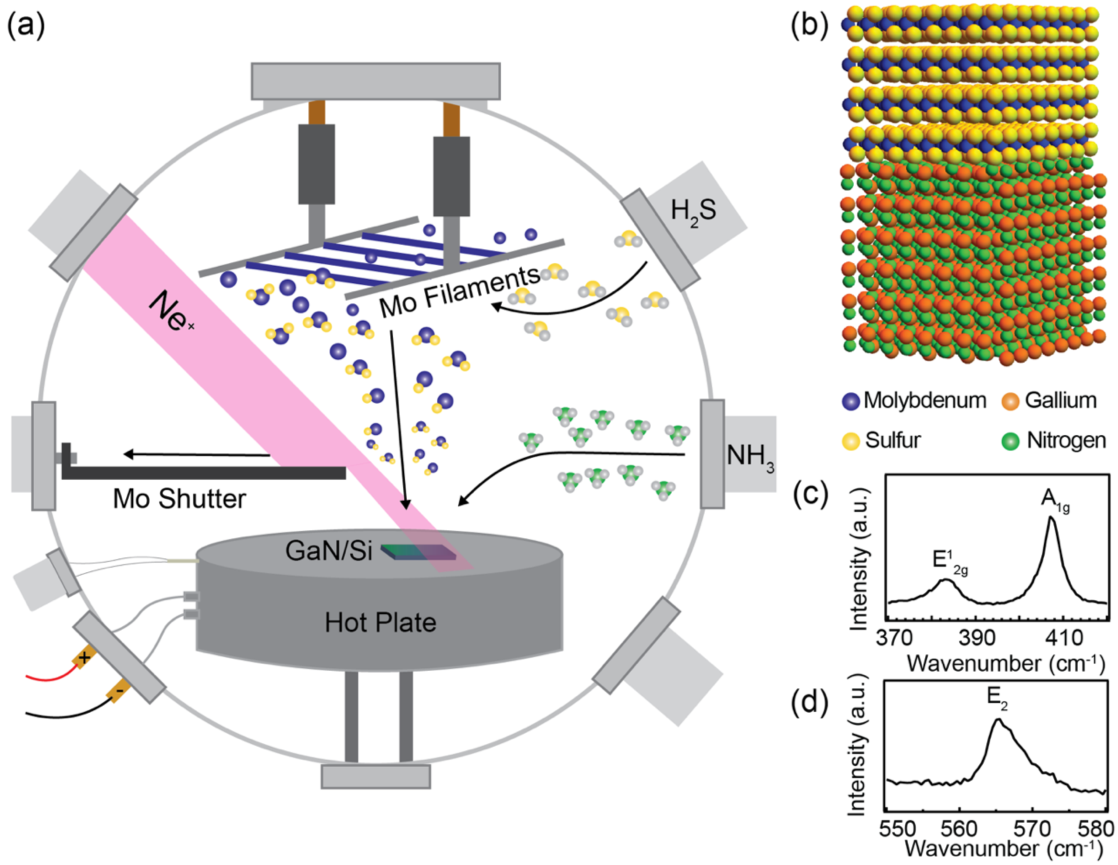

Figure 3.1 (a) Schematic representation of the growth reactor with different process steps indicated. (b) Atomic representation of stacked multilayer MoS_2/GaN structure. (c) Raman spectra of the MoS2 E^1_{2g} and A_{1g} modes and (d) the E_2 mode of the GaN substrate.

In this study, we use an ultra-high-vacuum compatible CVD growth technique described previously:[26] our system is capable of seamlessly (i) clean a GaN substrate by sputtering, (ii) then apply a high ammonia treatment to replace nitrogen lost during the sputtering process and generate a well-defined surface termination, and (iii) finally grow a MoS_2 film of controlled and uniform layer number all without breaking vacuum. Figure 3.1 shows a schematic representation of the system. So as to test a broad range of sputter fluences all in one run and without any variation in other growth conditions, a precision-controlled shutter is guided over the sample to generate a dose gradient. Measurement of the target current validates sputter fluence and beam alignment on the target.

MoS_2 deposition proceeds by exposing hot metallic molybdenum filaments (pyrometrically determined to be ∼1700 °C hot) to H_2S gas, resulting in the decomposition of the latter on the filament surface and generating MoS_x precursors with a vapor pressure far higher than refractory molybdenum. These precursors evaporate from the filaments, precipitate on the substrate that is held at 650 °C by a hot plate, and form a continuous MoS_2 layer. Colorimetric analysis of the reflection of the filaments from the sample allows us to monitor the layer thickness during growth and to end the deposition process precisely at the desired integer layer number.[26] XPS and LEED analysis was performed after transfer of the sample to a vacuum system equipped with a Spectra RS3000 analyzer, an OCI LEED system modified for computer control of gun and sample position, as well as ancillary instrumentation such as a sputter gun and evaporation sources.

The resultant MoS_2 film exhibits a Raman spectrum (Figure 3.1c) as expected from the literature and is otherwise free of optical contrast. The GaN substrate retains its characteristic Raman mode during overlayer growth (Figure 3.1d). No photoluminescence of MoS_2 is observed on the GaN substrate. Prior to MoS_2 growth, as-received n-type GaN substrates were cleaned using subsequent rinses in Acetone, isopropanol, and deionized water before being dipped into a piranha solution (30 mL H_2SO_4, 10 mL H_2O_2) for 5 min.

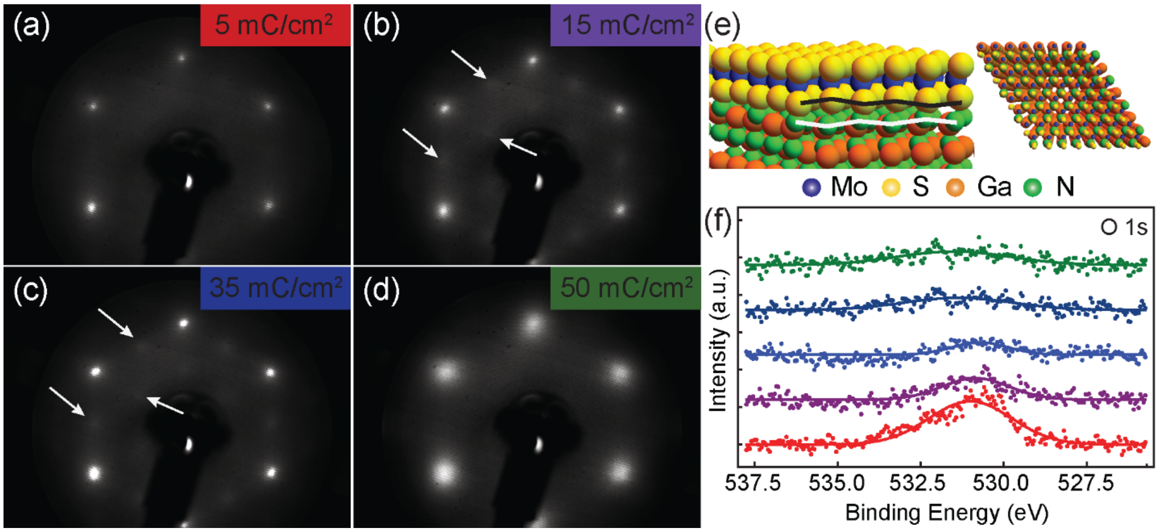

Figure 3.2 LEED patterns obtained at 100eV beam energy on (a) 5 mC/cm^2, (b) 15 mC/cm^2, (c) 25 mC/cm^2, and (d) 40 mC/cm^2 sputtered portions of a 1L MoS$_2$/GaN sample. A 2×2 superstructure is observed for intermediate sputter doses; the associate LEED spots are annotated by arrows; (e) DFT model of an N-terminated GaN/MoS$_2$ interface exhibiting a buckling of the top nitrogen layer (highlighted by the wavy line) with a 2×2 periodicity; (f) photoelectron spectroscopy of the oxygen 1s core level as a function of the sputter dose (same color code as labels in a-d).

To validate epitaxial growth and the quality of the GaN−MoS$_2$ interface, we performed low-energy electron diffraction (LEED) on a single layer of MoS$_2$ on GaN. LEED has a very high surface sensitivity[27] rendering work on a monolayer (rather than a multilayer) of MoS$_2$ necessary to gain structural information on the MoS$_2$/GaN interface. Figure 3.2 shows four LEED images across the sputter gradient of the GaN substrate from lower to higher sputter dosage; the sputter doses are indicated in each panel. At a low dose of 5 mC/cm^2, a sharp hexagonal diffraction pattern is visible (Figure 3.2a), which we attribute to the substrate periodicity (which is in good match to that of MoS2, especially given the known flexibility of the material).[28] Increase of the sputter dose to values between 15 and 35 mC/cm^2 results in a doubling of the periodicity (Figure 3.2b,c) generating a 2 × 2 pattern. Further sputter exposure results in broadening of the initial hexagonal spots, and the 2 × 2 spots disappear. We interpret this as the substrate surface becoming disordered, leading to less than epitaxial growth atop of it (Figure 3.2d).

There are several DFT simulations of the MoS_2/GaN interface available in the literature;[29, 30] generally, it is found that the surface energy of the Ga-terminated surface is higher than that of the N-terminated surface,[29] and that MoS_2 correspondingly exhibits higher adsorption energy on the former. For each termination, the optimal adsorption geometry places MoS_2 sulfur atoms on top of substrate top-layer atoms (Figure 3.2e). Our nitridation step directly prior to MoS_2 growth ensures that a nitrogen-terminated surface is present in our experiments. Using a six-layer stack of GaN and both 1L and 4L MoS_2 (Figure 3.1b) in a 2 × 2 lateral supercell (for a total of 144 atoms), we minimized the total energy for both the N- and Ga terminated surface testing a variety of adsorption sites, namely Ga-top, N-top, and intermediate sites, and obtained results consistent with the literature.[31, 32] We noticed that energy minimization on the favorable configuration on the N-terminated surface (Figure 3.2b) is unique among the superstructures in that it naturally results in a 2 × 2 superstructure with alternating top-layer substrate nitrogen atoms being depressed and lifted resulting in a similar buckling of the first layer sulfur layer of the MoS_2 overlayer. To ascertain the validity of this finding, we optimized the supercell until all forces were below 2 meV/Å both for the N-terminated surface, where the 2 × 2 superstructure is found, and the Ga-terminated one, where it remains absent. Notably, the vertical separation between the top nitrogen layer and the bottom sulfur layer is found to be only ~2.4 Å, smaller than the previously reported separation on Ga-terminated GaN on

MoS2 system.[32] We conclude that the S states (s, py, and pz) strongly hybridized with the N states (px, py, and pz). We interpret the buckling found in DFT as the origin of 2 × 2 superstructure spots in LEED patterns at an intermediate sputter dose. The presence of the 2 × 2 superstructure attests to a clean and well-ordered termination of the GaN substrate; were the substrate contaminated or rough, then a comparatively long-range order at the heart of the 2 × 2 reconstruction could not form and no 2 × 2 spots were observable in LEED.

XPS can serve as an alternative way to ascertain the cleanliness of the substrate. Our XPS measurements use a hemispherical analyzer read out by a 2D multichannel plate detector. One of the detector axes corresponds to energy dispersion in the hemisphere; the other to the spatial position on the substrate along the sputter gradient. Thus, slicing of the 2D data set along the energy direction at different locations provides us with spectra and their variation with sputter fluence. We performed such measurements across the sputter gradient for all relevant elements (Mo, S, Ga, N; impurities: C, O; valence band (VB) edge) both for 1L and 4L MoS_2 films. Figure 3.2f shows how the oxygen contamination of the surface decreases with sputter dose up to ∼25 mC/cm^2, when it is not identifiable anymore. We will discuss XPS results more in the context of explaining transport measurements.

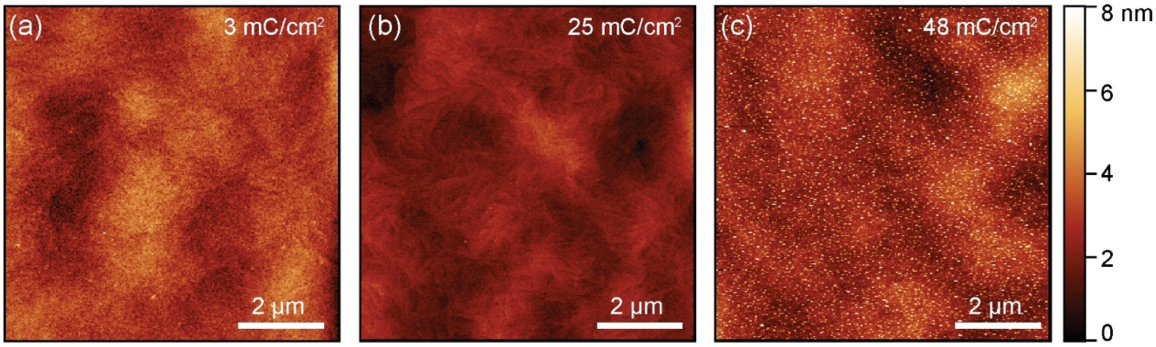

Figure 3.3 AFM images at different locations in a sputter gradient on a 1L MoS_2/GaN sample. (a) 3mC/cm^2, (b) 25 mC/cm^2, (c) 48 mC/cm^2. Conformal adhesion of the MoS_2 revealing a clear image of the underlying GaN terrace structure is only found at intermediate dose.

Atomic force microscopy (AFM) was used to characterize surfaces after film growth. Figure 3.3 shows three AFM images taken at locations of low, intermediate, and high sputter dose on 1L MoS_2 on a GaN sample. There is a marked distinction between areas of different sputter doses: at a low dose of 3 mC/cm^2, no clear image of the GaN terrace structure could be obtained (Figure 3.3a), presumably due to less than perfectly conformal substrate coverage caused by remaining substrate contamination. Imaging at a location with 25 mC/cm^2 sputter dose, substrate terraces are clearly defined under the MoS_2 overlayer attesting to good adhesion and conformal coverage. At an area with a local sputter dose of 48 mC/cm^2, we observe very small clusters on the surface that disrupt clear imaging and, presumably, uniform MoS_2 overlayer growth. We tentatively attribute the clusters to gallium sulfide or similar compounds formed during post sputtering sulfurization of a nitrogen deficient surface in the course of MoS_2 growth. We note that neon was chosen as sputter gas to assure a good mass match with second-period contaminants (such as oxygen and carbon, but also GaN nitrogen); yet it is unlikely to remove gallium atoms from the substrate.

3.3 Transport characteristics MoS_2/GaN diode and interpretation

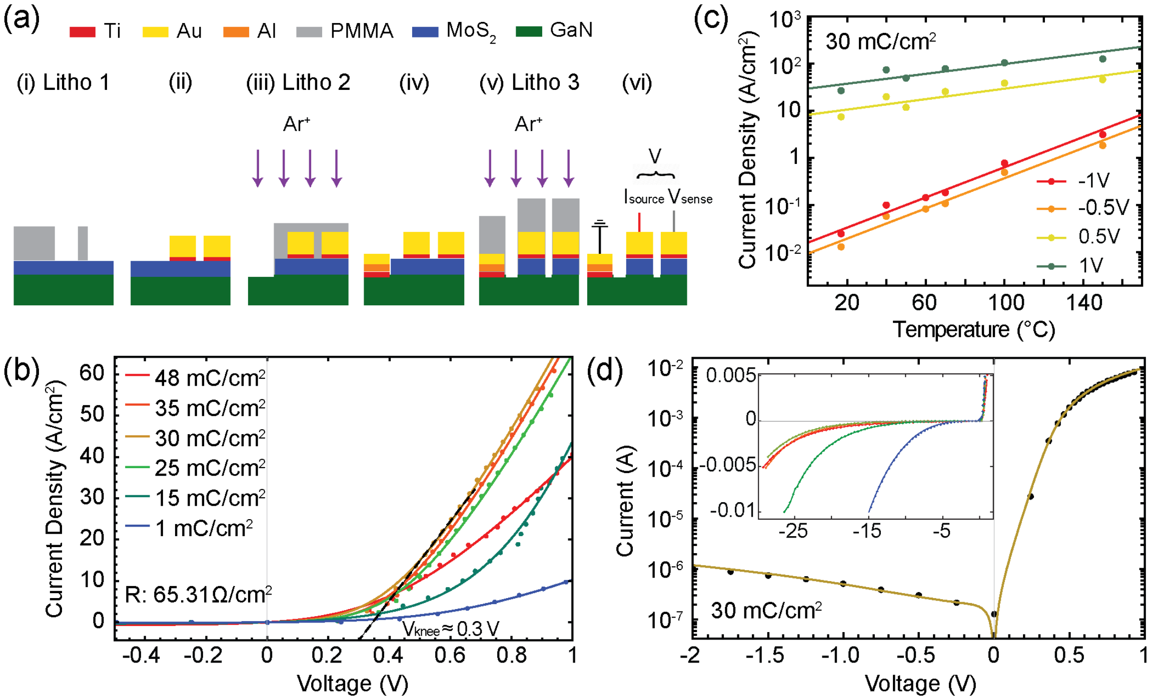

Figure 3.4 (a) schematic representation of 4L MoS_2/GaN device fabrication, (b) Current density vs. voltage for devices fabricated at locations with different sputter dose. A low knee voltage of 0.3 V is observed; (c) temperature dependence of the current density at different bias voltages, (d) a logarithmic plot of the I-V data for the optimal sputter dose can be fitted by an analytic function and reveals an on-off ration of ~10^5. The inset shows that reverse-voltage breakdown occurs at lower voltage for less sputtered interfaces.

To test the ramification of different interface preparations on the electrical properties, in particular the transconductance, of the MoS_2−GaN interface, we patterned devices on the substrate as shown in Figure 3.4a. Each device consists of a row of 120 by 120 μm Ti/Au pads placed on GaN and MoS_2/GaN. Fabrication proceeded in multiple steps of electron beam lithography: in the first lithographic steps, MoS_2 contact areas are defined (i) and a 5 nm titanium/50 nm gold stack is deposited (ii). After liftoff and deposition of a new resist layer, the GaN contact is defined and the MoS_2 material is removed via sputtering with argon at 3 keV (iii). Argon is chosen instead of neon for an optimal mass match with sulfur, molybdenum, and gallium, so as to prepare a clean and reactive GaN surface to support contact adhesion and reduce contact resistance. Without breaking the vacuum (base pressure 1×10^{-8} torr), a 5 nm of Ti and 50 nm of Al stack is deposited as described by Greco et al.[33] (iv). Note that no annealing occurred so as to preserve the MoS_2 layer. After Al deposition, the sample is transferred through air to a gold evaporator and a capping layer of 50 nm is applied. After liftoff, the third lithographic step begins by defining the area between the contacts (v). Subsequently, MoS_2 is removed here as well by Ar sputtering (vi).

The transport characteristics of MoS_2/GaN diodes are shown in Figure 4.4b with the voltage source from a Keithley 2400 sourcemeter applied to MoS_2 and ground to GaN. All measurements proceeded under voltage control in a three-terminal setup. To sense the voltage prior to the diode junction, we use a Keithley 6517a electrometer. The voltage V on the X-axis of Figure 3.4b is the difference between the voltage applied to MoS_2 and the observed electrometer voltage at the sense contact, thus approximating the voltage drop across the MoS_2/GaN stack while excluding contact resistance at the metal/GaN interface and most of the lateral voltage drop in the GaN layer.

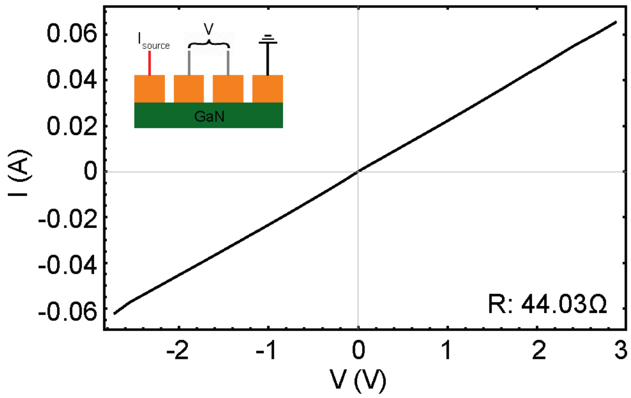

Figure 3.5 Electrical properties of the GaN contacts. Schematic representation of GaN device in the inset.

The Figure 3.5 shows the electrical properties of our GaN contacts and affirms that the features of Figure 3.4 do not stem from the latter. In particular, the exclusion of the metal/GaN interface in our measurement is motivated by an earlier study by Regan and et al.,[32] where it was demonstrated that the transport characteristics across a metal/1L-MoS_2/GaN stack is dominated by the metal/GaN interface for both the n- and p-doped GaN.

We find a marked diode behavior of the MoS2/GaN stack, whose details depend on the sputter dose of the interface. The forward direction of the diode is found, similar to previous studies,[34, 35, 36] for a positive voltage applied to MoS2, i.e., for electron transfer from GaN to the MoS2 layer. The turn-on or knee voltage (V_{knee}) of the diode is ~0.3 V, much lower than for Si-based diodes (0.6−0.8V) and rather resembling a Schottky diode (0.2−0.3 V). It is also much lower than the value reported in ref[36], presumably owing to the interface preparation. The diode has a high current density of ~100 A/cm^2 at 1 V. The current at −1 V bias is ∼5 orders of magnitude smaller than that at +1 V, i.e., the diode has an on−off ratio of $\sim 10^5$.

We find best diode behavior at sputter doses of ∼30 mC/cm^2; doses in excess of 40 mC/cm^2 lead to lower forward current, while sputter doses below 20 mC/cm^2 have a similar effect and also push the knee voltage (V_{knee}) toward larger values. Low sputter doses also lead to reverse breakdown at a lower voltage (inset of Figure 3.4d).

We attribute the high dose behavior to a rougher MoS_2/GaN interface. As can be seen from Figure 3.3c, at a high sputter dose, AFM observes the formation of small clusters on the substrate, presumably reducing the area of the perfect interface between the substrate and MoS^2 overlayer. This reduces the active area of the diode and, thus, its forward current. We attribute the deterioration of the properties at low sputter dose to the presence of oxygen in the interfacial layer changing both its electronic character and preventing optimal adhesion/epitaxy. Exfoliation of MoS_2 onto GaN has been shown to lead to diodes with a knee voltage of 1−2 V and an on−off ratio at ±5 V of $\sim 10^3$, almost 2 orders of magnitude smaller than those sputtered at ∼30 mC/cm^2.[34] Other growth studies either found results[35] similar to exfoliation MoS_2 junctions or high transconductance but no pronounced blocking behavior,[37,38] which may be interpreted as breakthrough at very low reverse bias, similar to the trend we observe for low sputter doses.

Figure 3.4d includes a fit of the measured current (I) data using the Schottky model of a diode: $I = I_S(\exp[V/(nV_T)]\text{-}1)$ with I_S the scale current, n the ideality factor, and V_T the thermal voltage taken as $V_T = kT/q$ =25.85 mV, with k the Boltzmann constant, T the absolute temperature, and q the absolute of the electron charge. We expanded the Schottky model by two terms, replacing V by $V\text{-}I{*}R$ to account for a series resistance R of the junction[39] and an additive $V/Vp \times Ip \times (1\text{-}\exp[V/Vp])$ term[40] to account for a tunneling current Ip at reverse voltage Vp through the thin diode layer:

$$I = I_S\left(e^{V-I\times R/_{n\times V_T}}\right) + {}^{V}/_{V_P}\, I_P\left(1 - e^{V/_{V_P}}\right) \qquad (1)$$

Fitting the experimental data reveals a series resistance of ~50 Ohm, an ideality factor of 1.8, a scale current of 20 nA, and the tunneling behavior described by 2 μA at 2.4 V for I_P and V_P, respectively. These are excellent values for our prototypical device geometry.

Temperature-dependent data on transconductance were obtained both for forward and reverse bias (Figure 3.4c). We observe a marked distinction of the thermal behavior at forward and reverse bias, as expected for a diode as thin as the one fabricated here. Figure 3.6 shows an Arrhenius-type fit of the current density J = A exp(Eb/kT) with a prefactor and Eb an energy barrier. At reverse bias, we find Eb to be ∼380 meV, in line with the knee voltage. At 0.5/1.0 V forward bias, we find values of ∼140/110 meV.

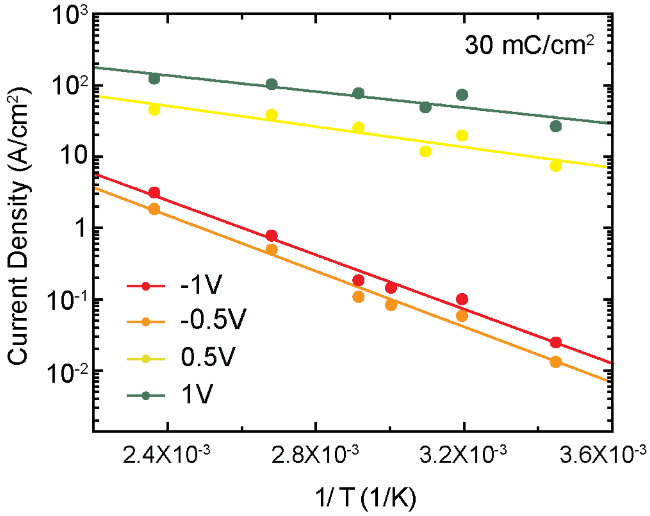

Figure 3.6 Temperature-dependent current data (from Fig. 3.4c) plotted in the Arrhenius style vs. 1/Temperature. Fitting with A×exp(E_b/kT) results in barriers of ~380 meV for reverse direction, in good agreement with the knee voltage and the CB band separation (shown in Fig. 3.4 and 3.7 respectively), and ~140 meV/110 meV for 0.5V/1V in forward direction.

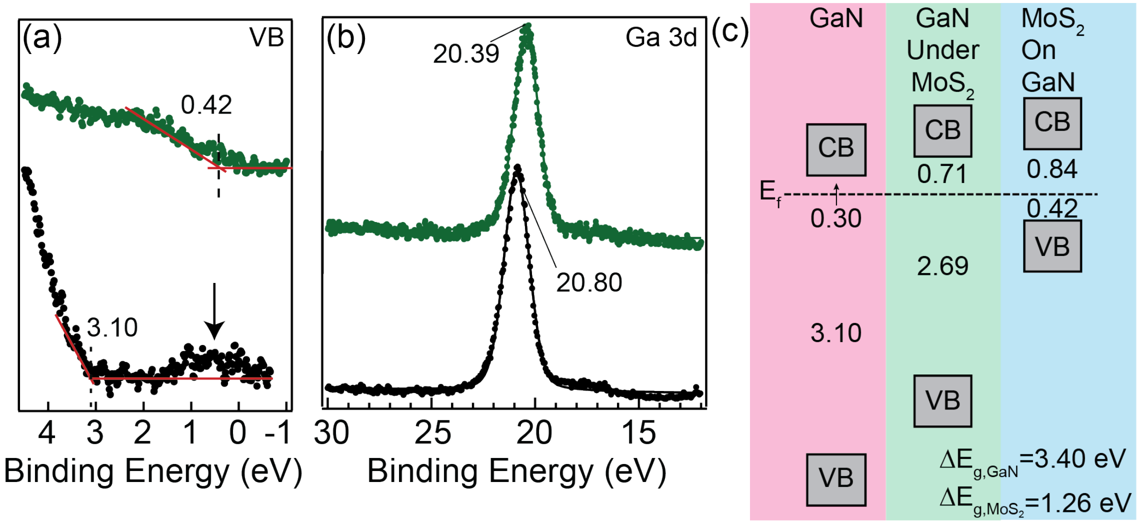

Figure 3.7 (a) Valence band (VB) edge XPS spectra of nitridated GaN prior to (bottom) and after (top) 4L MoS_2 growth. The respective band edges are indicated. Additional, density of state from the nitrogen termination is observed near the Fermi energy (E_f) on bare GaN(arrow); (b) GaN 3d state before (bottom) and after (top) MoS_2 overlayer growth. The upshift shows surface band bending associated with charge transfer to the GaN; (c) energy diagram of the VB and conduction band (CB) position of GaN prior to 4L MoS_2 deposition (left), after 4L MoS_2 deposition (middle), and of the MoS_2 layer (right) based on known band gaps indicated.

How can we understand transport characteristics? Note that n-type behavior is expected both for the GaN substrate (through doping) and the MoS_2 layer, as is typically for CVD MoS_2 material. Thus, a pronounced diode behavior is not necessarily expected. To understand its origin, it is helpful to take another look at XPS data: Figure 3.7a compares the valence band (VB) region of bare GaN after nitridation (bottom) and following 4L MoS_2 deposition (top). On bare GaN, we find the VB edge at ~3.1 eV, suggesting n-type GaN material consistent with the commercial supplier specification. In addition, we observe some density of states near the Fermi edge (arrow in Figure 3.7a), which we attribute to unsaturated dangling nitrogen bonds at the nitrogen-terminated surface. Figure 3.8 shows the element-projected density of state (pDOS) for a 4L MoS_2/GaN interface (six layers of GaN). Nitrogen-originating density of states is found right below the Fermi level in the semiconductor gap.

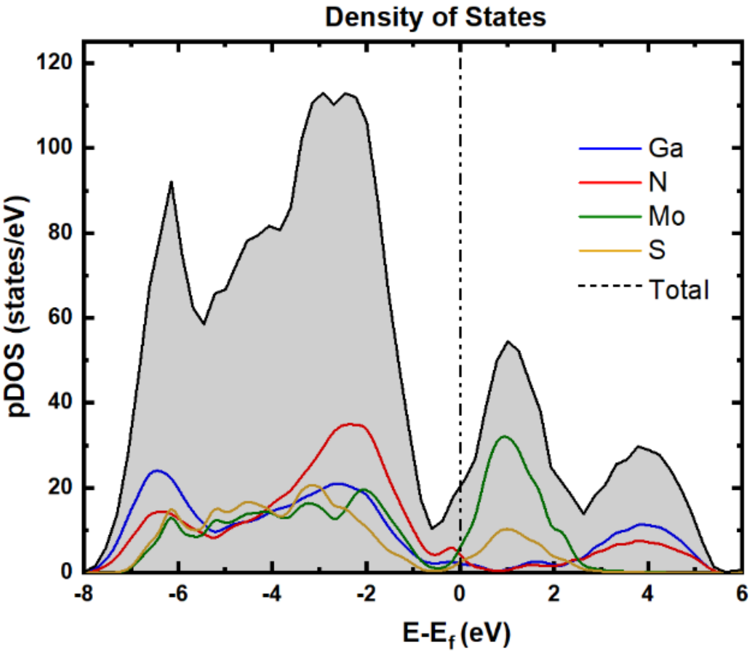

Figure 3.8 Element-projected density of state (pDOS) obtained from minimizing a 4L MoS$_2$/ 6L GaN interface. Nitrogen-derived density of states is found directly at the Fermi-level representing the nitrogen-sulfur interaction that give rise to the 2×2 reconstruction. We note that our DFT simulation does not represent overall band alignment faithfully, likely because of absence in the model of (i) explicit *n*-doping of the GaN substrate, (ii) native *n*-doping of the MoS$_2$, and termination of the bottom Ga-layer of the GaN slab.

The MoS$_2$ VB edge is found at ~0.4 eV below E$_F$, closer to the Fermi energy than for material grown on SiO$_2$[41] and indicating a material that appears like a p-type semiconductor (4L MoS$_2$ has a band gap of 1.26 eV, so for the VB edge at 0.4 eV below E$_F$, the Fermi energy is below midgap). We attribute this observation to charge transfer at the interface.

To understand the interface charge transfer, we address the Ga 3d peak. Prior to MoS$_2$ deposition, we find the Ga 3d state at ~20.8 eV binding energy, well in line with typical values for GaN. After MoS$_2$ deposition, we observe an upshift by ~0.4–20.4 eV.

This indicates surface band bending by 0.4 eV in the course of MoS_2 deposition, i.e., charge transfer from MoS_2 to GaN. As MoS_2 is typically natively n-type, we interpret this finding as to the n-type carriers of the 4L MoS_2 CB dropping into the GaN CB, thereby shifting the energy of the GaN surface and the Ga 3d state up, i.e., upward surface band bending. In this process, MoS_2 loses its n-type character shifting the Fermi level below midgap.

Figure 3.7c shows the VB and CB edge positions as obtained from the XPS measurements and calculated based on literature band gap values, respectively. Assuming that the GaN VB edge upshifts in sync with the GaN 3d state, the MoS_2 CB edge comes to lie 0.1–0.2 eV above the GaN CB edge, corroborating the notion of n-type carriers dropping from MoS_2 into GaN. We note that this mechanism also explains the absence of photoluminescence for MoS_2 on GaN: excitons rapidly split by transfer of the excited carrier into GaN CB.[42]

As a consequence of this band alignment, the MoS_2/GaN diode resembles much more a Schottky diode of an n-type material than a pn-juction; all transport takes place in the CB. The knee voltage of 0.3 eV is in reasonable agreement with the MoS_2-GaN CB offset of 0.1–0.2 eV to enable electron transport from GaN CB to MoS_2 CB and into a metal contact. It also agrees well with the barrier for reverse current found from temperature-dependent measurements on the diode.

Finally, we seek to corroborate this finding by analyzing the charge and potential distribution in our computational supercell. Figure 1b shows its thickness; each supercell layer contains 2 × 2 GaN or MoS_2 unit cells and there are four MoS_2 and six GaN layers in our calculation. We caution that our DFT simulation does not represent overall band alignment faithfully, likely because of absence in the model of (i) explicit n-doping of the GaN substrate, (ii) native n-doping of the MoS_2 layer, and (iii) termination of the bottom Ga layer of the GaN slab. However, we can still evaluate the charge transfer directly at the GaN/MoS_2 interface. This will lead to a built-in electrical field and potential that can affect the transfer characteristics of 2D/three-dimensional (3D) heterostructures.

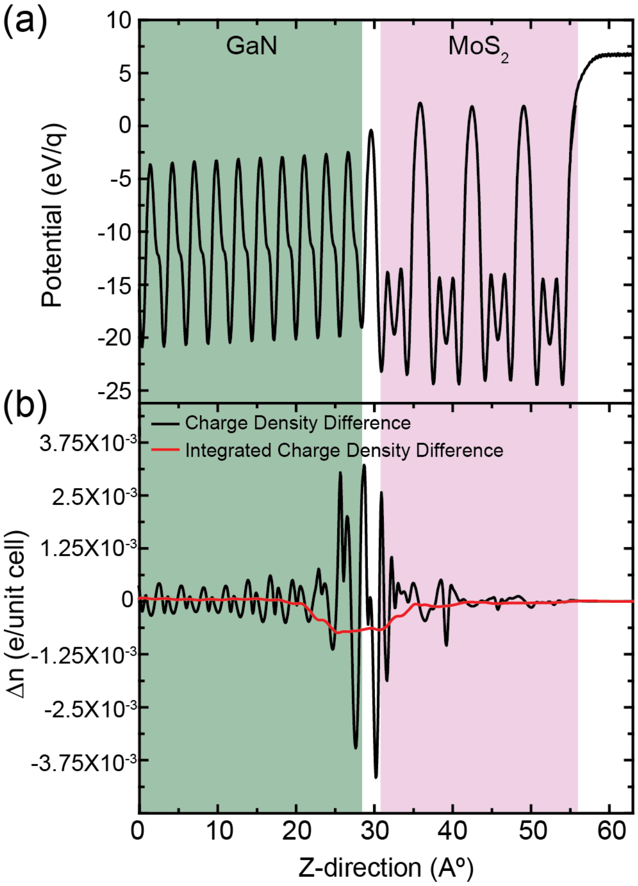

Figure 3.9 (a) Planar potential variation at the GaN/MoS_2 interface: upward band bending is observed for GaN toward the interface; (b) Interface charge transfer: the charge density difference (black) of the combined MoS_2/GaN system as compared to the separated system and its integral from the right (red). Visible is charge transfer from the MoS_2 layer and particularly the interface region to the GaN bulk.

Figure 3.8 illustrates the electrostatic potential and charge difference profiles along the z-direction, i.e., normal to the heterostructure. As can be seen in Figure 3.8a, the interfacial built-in potential throughout the vdW interface, mainly due to the charge reconfiguration at hybridized S and N states, leads to an upward slope in the GaN region toward the interface, i.e., a surface band bending consistent with the experimental finding. In addition, the local electrostatic potential around the sulfur atoms at the interface in the heterostructure is reduced by 4 eV, as compared to the isolated 4L MoS_2 system, leading to a lower barrier for electron migration across the interface. The charge redistribution is visualized in Figure 3.8b as the difference between the charge density of the isolated layer slabs and the combined ones. Significant deviation (black line) from isolated slabs in the vicinity of the interface attests to the chemical interaction here manifest in the 2 × 2 superstructure. The integrated charge density difference (red line, using a 10 Å width rolling average) shows charge density loss throughout the MoS_2 film amplified directly at the interface and charge gain by the GaN substrate except directly at the interface, where direct chemical interactions between the nitrogen and sulfur layer are observed. This net charge transfer was also predicted from the XPS data.

To quantify and validate the MoS_2/GaN charge transfer, we performed a Bader charge analysis[43] across the interface. The S atoms at the interface lose on average 0.025 electron charges each, consistent with the charge profile picture. Most of the transferred electrons are acquired by the surface N-atoms yet N-atoms in neighboring layers also acquire a small fraction of electrons, which is also evident from the nonzero charge profile feature in the GaN region, away from the surface in Figure 3.8b.

In conclusion, we find that careful optimization of the interface allows the fabrication of high-quality GaN/MoS_2 diodes with a low knee voltage and high on–off ratio. Because of the device geometry employed here, no meaningful high-frequency measurements are feasible; however, all results suggest that a good high-frequency response is expected. Future research seeks to extend this work to GaN/MoS_2/GaN npn-heterojunction bipolar transistors. In this context, it is an important outcome of the current work that MoS_2 loses its native n-type character simply by the interface interaction at the N-terminated GaN substrate and that no further treatment of the MoS_2 (e.g., such as niobium doping[44]) may be necessary to attain such a goal. Our findings highlight the importance of atomistic control of the interface, even for 2D vdW materials, which are generally assumed to be more robust to interface contamination than classic epitaxial systems such as GaAs/GaAlAs.

Chapter 4: Growth of GaN on MoS_2

4.1 Motivation

The existence of bandgaps in transition metal dichalcogenides (TMDs) such as molybdenum disulfide (MoS_2) offers an attractive possibility of using these layered materials in various device applications.[45,46] Gallium nitride (GaN) initially introduced into semiconductor technology as a wide-band-gap material able to provide blue light-emitting diodes[10] has found a number of additional applications for power conversion.[11] A primary challenge in this material has been the difficulty of obtaining native GaN on large lattice-mismatched substrates such as Si and sapphire. There has always been a desire to seek lattice-matched substrate for GaN growth. For this purpose, molybdenum disulfide (MoS_2) was considered as an ideal substrate since GaN and MoS_2 possess in-plane lattice mismatch of only ~0.8%.[19] The close lattice match between MoS_2 and GaN has led to an interest in the epitaxial relationship and electrical properties of heterojunctions.

Vertical devices based on 3D-GaN / 2D-MoS_2 / 3D-GaN hetero structures have the potential to take advantage of the conventional 3D semiconductors and the unique properties of thin 2D films. The thin 2D-MoS_2 TMD provides for high-speed operation and the vertical structure of the electronic transport allows for a large surface area and thus high current.[47] As an initial step for GaN/MoS_2/GaN hetero bipolar transistor (HBT), we found low turn-on voltage Schottky-diode behavior of a MoS_2/GaN junction by optimizing the GaN substrate before growing MoS_2.[48] It will allow us to grow GaN on high quality MoS_2/GaN structure and lead to high performance of HBT.

To date, there are only a few reports about the growth of GaN films on MoS_2. The first report by Yamada et al. has demonstrated the growth of GaN on bulk MoS_2 by molecular beam epitaxy (MBE).[49] There were recent reports to grow GaN on single layer MoS_2 by plasma-enhanced atomic layer deposition[50] and grow MoS_2 on GaN by plasma assisted Molecular beam epitaxy.[51] However, the study of in situ growth of GaN and MoS_2 and the fabrication of GaN/MoS_2/GaN heterojunction bipolar transistors has not been explored. Also, among the studies, there is an issue that the MoS_2 film was found to be removed during the GaN growth.[19,51]

In this project, we aimed to optimize the growth mechanism of GaN on MoS_2. We use a high vacuum CVD MoS_2 growth technique described previously:[26] MoS_2 deposition proceeds by exposing hot metallic molybdenum to H_2S gas. After growing MoS_2, we use a unique growth mechanism of GaN in-situ using Ga effusion cell and filaments for activating NH_3 gas, which allows the clean surface of MoS_2 to grow well on GaN substrate. In order to grow good quality GaN film on MoS_2, we have tried a number of growth mechanisms by using various parameters: substrate temperature, Ga evaporation rate, filaments current, and high voltage for filaments.

This project aimed to optimize the growth mechanism for high quality GaN and in situ epitaxial growth of GaN on MoS_2/GaN without removal of MoS_2. The structural quality of the GaN/MoS_2 films was evaluated through X-ray photoelectron spectroscopy (XPS), Raman spectroscopy and Low-energy electron diffraction (LEED). This work will be extended to GaN/MoS_2/GaN heterojunction bipolar transistors.

4.2 MoS_2 Growth and Optimization of GaN Growth Mechanism

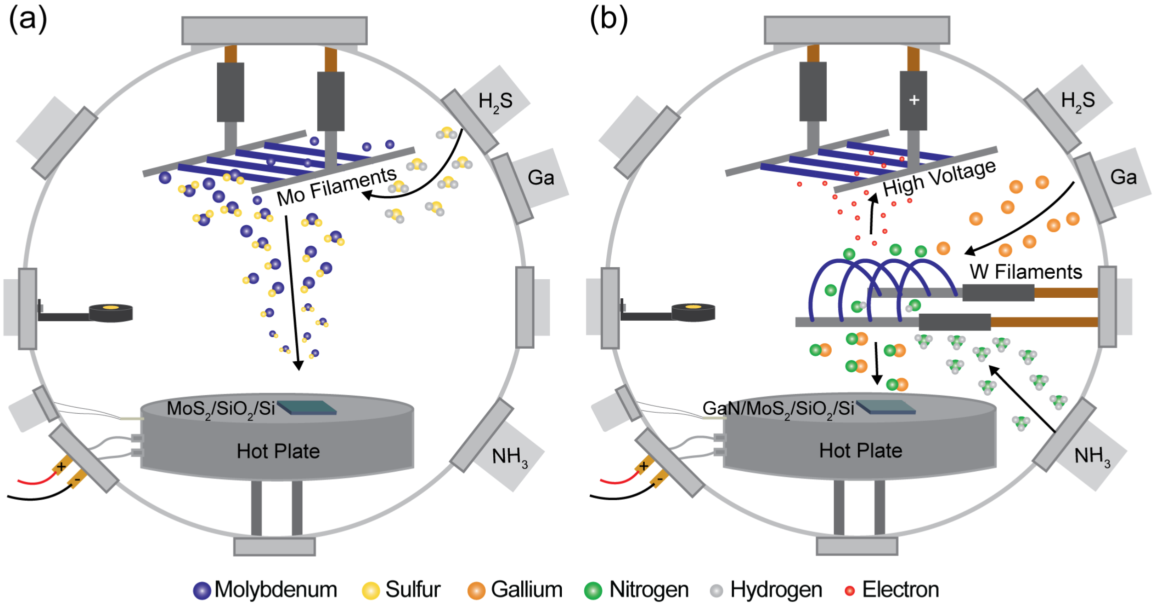

Figure 4.1 Schematic representation of the growth reactor with different process steps indicated (a) Growth of MoS_2 (b) Growth of GaN

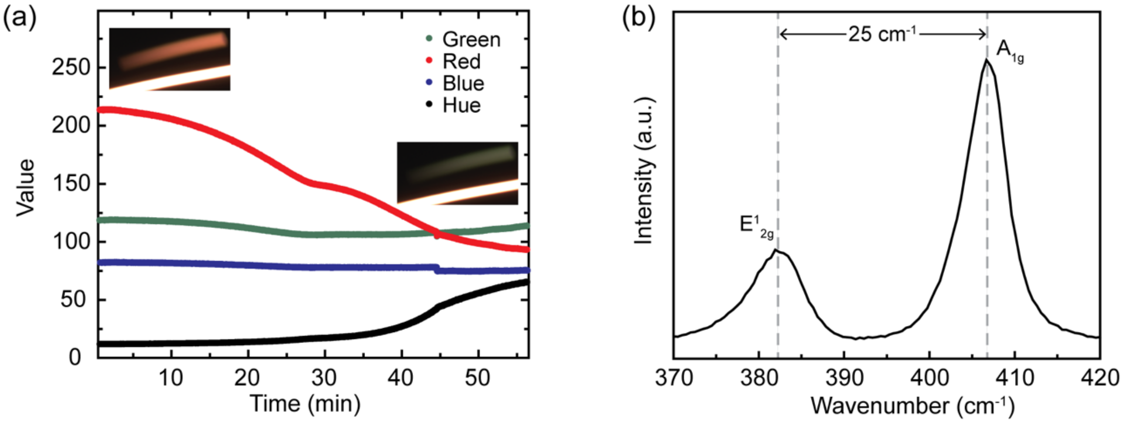

Figure 4.2 (a) RGB values and Hue of the Mo filament reflection during film deposition (b) Raman spectra of MoS_2 E^1_{2g} and A_{1g} modes. The peak separation is 25 cm^{-1}.

A vacuum chamber is equipped with a rough pump and a turbo pump to achieve high vacuum at 10^{-7} torr. It set up a hot plate style heater and a leak valve for H_2S and NH_3, as shown in Figure 4.1. Four separate molybdenum wires with a diameter of 0.5mm provide the molybdenum source. The first step of growth is to ramp up the hot plate temperature to ~750 °C and hold 15 mins to remove organic contaminants and water from the sample. Next, we decreased the hot plate temperature to 650 °C as MoS_2 growth temperature. Once the desired temperature is reached, H_2S gas is dosed to $4x10^{-4}$ torr. The molybdenum filaments are resistively heated until ~1700 °C hot, resulting in the decomposition of the filament surface and producing MoS_x precursors, as shown in Figure 4.1a. The MoS_x precursors evaporate from the filaments at a substrate temperature of 650 °C and form a continuous MoS_2 layer.[26] The MoS_2 growth is monitored by colorimetric measurements of the reflection of the filaments from the sample, allowing us to end the deposition process at the desired number of integer layers, as shown in Figure 4.2a. The thick MoS_2 film that I used is 6 layers based on the Hue of the Mo filament reflection and the separation of two Raman modes (~25cm^{-1}) [Figure 4.2b].

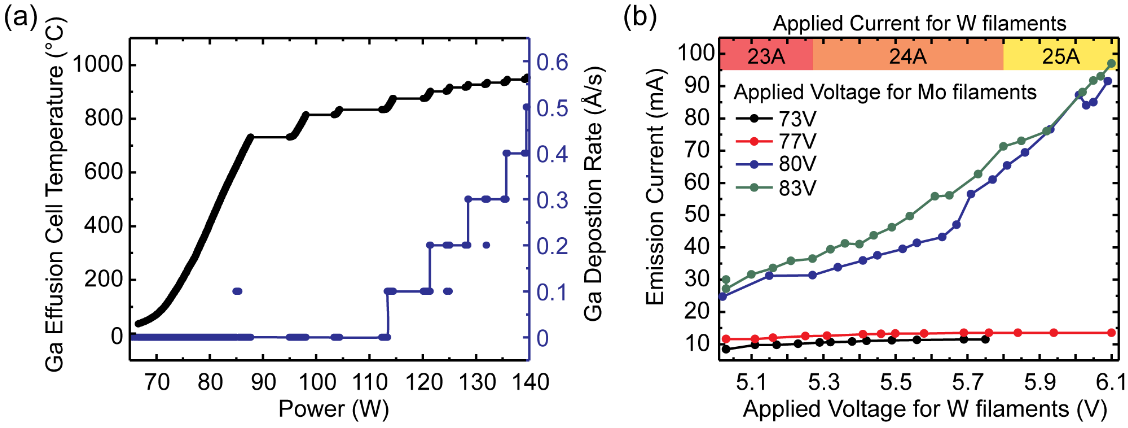

Figure 4.3 (a) Deposition rate and Ga effusion cell temperature as a function of applied power (b) Emission current as a function of the applied voltage for tungsten filaments.

The growth of GaN starts in-situ right after the growth of MoS_2, preventing the MoS_2 surface from being contaminated. GaN deposition proceeds by using a Gallium effusion cell and activating NH_3. In order to grow GaN, I tried several growth methods by changing parameters such as the hot plate temperature, Ga deposition rate, filament current and voltage. The Ga deposition rate is monitored by a thin film thickness monitor connected to a quartz crystal microbalance (QCM) sensor on the left side of the chamber, as shown in Figure 4.1b. Figure 4.3a shows deposition rate and Ga effusion cell temperature as a function of applied power. The growth starts depositing Ga layer first at different hot plate temperatures from 200 to 650°C to prevent degradation of the MoS_2 film for 10 min. NH_3 is dosed at ~ $4x10^{-3}$ torr and is activated by tungsten filaments. Tungsten filaments are ramped up, resulting in NH_3 decomposition. Molybdenum filaments with high voltage applied attract electrons from the NH_3 decomposition and allow emission current to be read. The activated nitrogen is combined with Ga and produces GaN. I used the emission current from 60 to 95 mA to activate $NH_{3,}$ as shown in Figure 4.3b. GaN layers are grown for 30 min, and GaN thickness is 36 nm based on when Ga is deposited at 0.2 A/s.

4.3 Characterization of GaN on MoS_2

Raman spectra were measured to monitor the impact of the GaN growth conditions on the MoS_2. As shown in Figure 4.4a, GaN growth under 400 °C and 300 °C substrate temperatures, MoS_2 remain stable at 300 °C from MoS_2 E^1_{2g} (382cm^{-1}) and A_{1g} (406cm^{-1})

modes, but MoS_2 peaks disappeared at growth temperature 400 °C, suggesting loss of crystallinity of the MoS_2 film. It is difficult to observe GaN E_2 (~566 cm^{-1}) and A_1(~734 cm^{-1}) peaks. It assumes the poor quality of GaN or peaks overlapped with other peaks due to less intensity, comparing that E_2 mode of GaN reference (NTT-AT, Si-doped 300nm GaN) has less intensity and 12.5% intensity of Si peak. To figure out the strategy of preservation of MoS_2 and high crystallinity GaN, we first focused on high quality GaN on c-plane sapphire at higher temperatures from 800 to 1000 °C referred to in literatures.[52, 53] Figure 4.4c shows Raman peak of GaN grown at 800 °C and reference GaN on Sapphire (NTT-AT). We observed E_2 and A_1 peaks even though the peak position is ~5 cm^{-1} off from the reference peak, meaning that we still need to optimize. We ensure that high temperatures allow us to grow GaN crystallization, and that gives us the direction to make freestanding 2D layers from high temperatures. WS_2 is one of the 2D layers that can be produced at a higher temperature than MoS_2 and lattice-matched to GaN (lattice mismatch of ~1%[14]), appearing as a promising substrate for the growth of GaN at high temperatures.

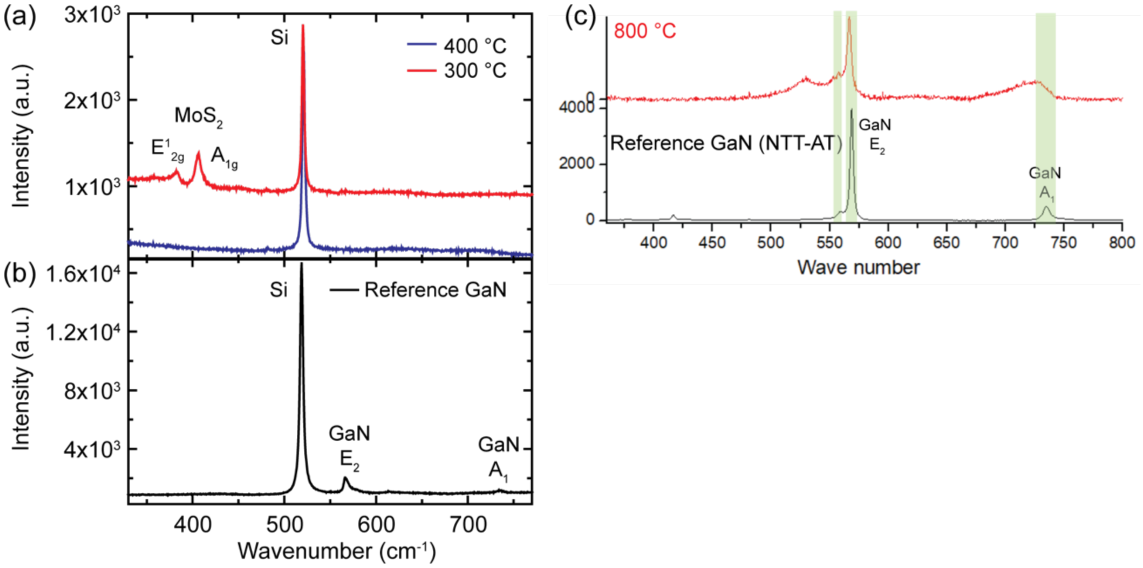

Figure 4.4 Raman spectra for (a) growing GaN on MoS2 under different growth Temperature, (b) Reference GaN (NTT-AT, 300 nm GaN), (c) growing GaN on Sapphire at 800 °C

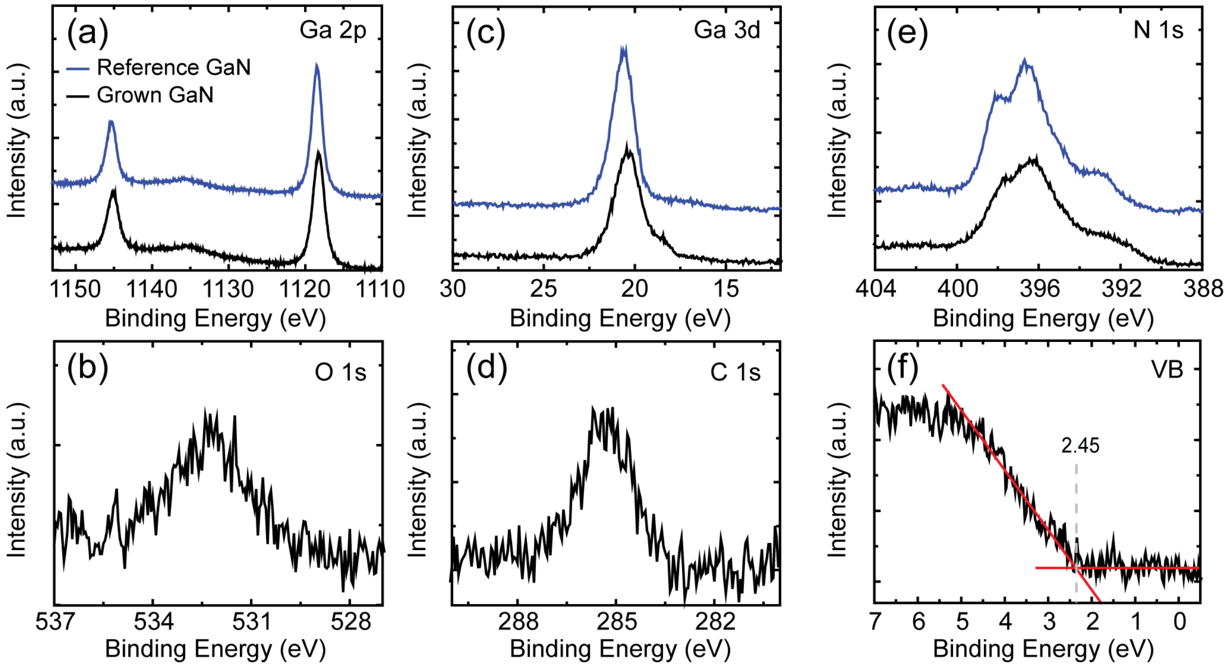

Figure 4.5 XPS spectroscopy of GaN (a) Ga 2p, (b) O 1s, (c) Ga 3d, (d) C 1s, (e) N 1s, (f) Valence band.

X-ray photoelectron spectroscopy (XPS) investigated the composition of the GaN films grown at 300 °C in which MoS_2 film is stable based on Raman spectra. Figure 4.5 shows the XPS spectra of Ga 2p, Ga 3d, N 1s, O 1s, C 1s, and valence band. In Ga 2p and Ga 3d orbitals, we observed the same peaks as reference peaks of GaN (NTT-AT, 300 nm GaN). Furthermore, XPS spectra of Ga 3d are divided into three regions, Ga-Ga, Ga-N and Ga-O bonding of grown GaN and Ga-N peak around 20.4 eV has a strong peak intensity among three regions. The N 1s peaks were de-convoluted into four contributions in all cases: i.e. an $N–H_2$ ionization peak (397.7 eV), an N–Ga ionization peak (396.2 eV) and two Auger Ga peaks (395.5, 393.2 eV).[54] We observed the same peaks as reference GaN, which indicates NH_3 is decomposed and the activated nitrogen bound with Ga. O 1s peak indicates low oxygen contamination during growth, which is advantageous for growing in situ MoS_2 and GaN without breaking vacuum. We found the VB edge positions at ~2.45eV, suggesting n-type GaN material. In addition, the ratio of Ga and N atomic weight percentages (atom wt%) of the surface species (Ga/N=0.5) were determined using peak areas and sensitivity factors for N 1s and Ga 3d, which are 0.44 and 0.49 eV for reference GaN and grown GaN, respectively.

In conclusion, we attempted to grow GaN on MoS_2 by using a Ga effusion cell and N provided by high voltage and tungsten filaments to activate NH_3. It is challenging to grow good quality GaN epitaxially without damaging MoS_2. From Raman results of GaN produced at a high temperature of 800 °C, we conclude that the growth of high crystallinity GaN needs a higher temperature and lattice matched WS_2 for freestanding from heat as well as epitaxial growth. Once a mechanism is optimized for epitaxial GaN on 2D layers/GaN, we can make a GaN/2D layers/GaN hetero bipolar transistor application, which leads to an analysis of the electrical characteristics and goals to achieve the amplifying behavior.

Chapter 5: WS_2/MoS_2 Vertical Heterostructure

The following chapter contains excerpts from “Photoluminescent Substrate-Scale 3R WS_2/MoS_2 Heterostacks on GaN” by **Yang, H. I.**, Ning,Y., Jin,J., Juarez, M., Henshaw, J., Azizur-Rahman, K., Flores, B., Meneses, N., Yadav, P. R., Villarreal, S, Hill, M. E., Sorger, V., Mounce, A., and Bartels, L. (in review)

5.1 Motivation

Since the single-layer direct-bandgap nature of transition metal dichalcogenides (TMDs) was discovered more than a decade ago,[46,55] these materials have seen intense investigation.[56,57] It is widely assumed, and corroborated by theory,[5–7] that only the single-layer-form of these materials in the 2H polytype offers a direct and significantly-widened bandgap as well as bright photoluminescence, although over the years a number of publications[61–66] have found deviating behavior based on material preparation. The synthesis of TMDs is maturing from tube-furnace chemical vapor deposition of populations of triangular islands,[67–69] to high-vacuum particulate-free large-area homogeneous growth.[26,70] In one approach, developed by some of us, a hot transition metal filament is exposed in high vacuum to a sulfur precursor, resulting in the volatilization of MS_x

precursors (M, transition metal; x=1-2) and subsequent precipitation onto a heated substrate where a TMD film is formed.[26,71] On GaN, whose lattice constant of 3.189 Å[12,72,73] closely matches that of MoS_2 (3.160 Å)[14,72] and WS_2 (3.153 Å),[14,72] a pseudo-epitaxial TMD film results that exhibits clear diffraction patterns.[26,74,75] Here, we show that if during deposition we alternate the metal source between molybdenum and tungsten, the film will dominantly grow as 3R TMD, exhibit bright photoluminescence, and a band gap typically associated with monolayer films.

A very large number of publications detail the growth of TMD materials using both tube furnace and reactor-style processes.[26,67–70,75–77] To our knowledge, the closest in film properties to our films result from work by Jo et al.,[78] where over days a substrate is exposed to alternating metal-organic transition-metal precursors leading to a clearly layered film. More recently, the properties of 3R MoS_2 have attracted increased attention[8] because of their catalytic,[79,80] piezovoltaic,[81] and other[82,83] properties. From a technological perspective, the use of monolayer films is challenging because the slightest inconsistency of their thickness – or the slightest defect in them – fundamentally changes the material. To the best knowledge of the authors, no commercially viable process in the semiconductor industry relies on a single layer of a material. This underscores the need to transfer the exciting single-layer properties of TMDs to thicker films.

5.2 Experiments

The TMD growth method employed in this study is shown schematically in Figure 5.1a; it takes just a few minutes per layer. Figure 2.1 shows a photograph of the growth chamber. To facilitate epitaxial growth, we first sputter a commercial [NTT Advanced Technology] GaN/Si substrate with low-energy neon ions before nitridating the surface with ammonia at 750 °C under activation by a DC plasma. Passing a current density of 320 A/mm^2 and 730 A/mm^2 through a set of four tungsten and molybdenum wires of 0.50mm and 0.28mm thickness, respectively, results in their bright glow, which is monitored by a video camera and kept constant by three color pyrometry during the process. Concomitant exposure of the filaments to H_2S then leads to desorption of volatile MS_x (M=Mo,W) species that are precipitated onto a heated GaN substrate. Using a piece of 300nm SiO_2/Si as a reflector, we monitor the ratio of the filament glow reflected in the green to that in the red spectral region, which can be used as a film thickness monitor.[26] Cycling between tungsten and molybdenum filaments, we grow as many layers as desired while maintaining in-plane order.

Figure 5.1b,c shows the resultant heterostack schematically and by cross-sectional element-sensitive transmission electron microscopy (TEM). We observe PL on heterostacks of at least 6 films (i.e., WS_2-MoS_2-WS_2-MoS_2-WS_2-MoS_2-GaN) even if each film exceeds a monolayer. Notably, neither single-layer MoS_2 nor single-layer WS_2 nor thick layers of these materials exhibit appreciable photoluminescence when deposited on GaN; the former is due to exciton dissociation at the TMD/GaN interface.[26,42] Raman spectroscopy [Figure 5.1d] ascertains that the layers are separated and that intermixing of the transition metal does not occur to a significant extent.[84] In the following, we provide additional characterization of the heterostacks and seek to explain their photoluminescence behavior.

Transmission Electron Microscopy (TEM)

For transfer to TEM imaging, the sample was capped with a sequence of titanium and platinum overlayer. The TEM specimen was prepared using a Tescan GAIA3 scanning electron microscope (SEM) equipped with a focused ion beam (FIB). A lamella was prepared from a region near the center of the sample. The high-resolution STEM images were carried out using a JEOL ARM300 TEM at 300 kV. The EDS data were collected using a JEOL dual EDS detector.

Device fabrication

Device fabrication used C-type PMMA electron resist. The first lithographic step defines the contact pads on the heterostacks that are after development exposed to 15nm Ti and 200nm Au. Following liftoff, the contact pads for GaN were defined the same way using a sequence of sputtering followed by stack of 5nm Ti/ 60nm Al/50nm Au for ohmic contact behavior. Argon sputtering at 3 keV for one hour is used to remove the material between the contacts.

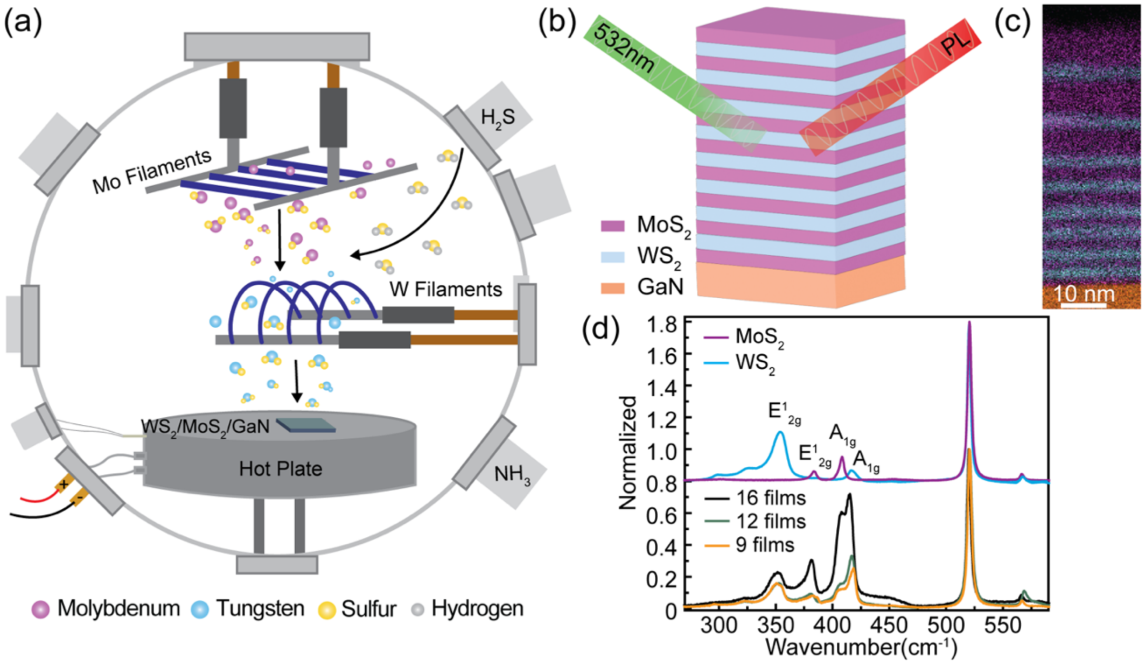

Figure 5.1 Schematic representation of (a) high vacuum film growth method and (b) photoluminescence emission from heterostacked WS$_2$/MoS$_2$ under a 532nm laser excitation. (c) Cross-sectional EDS images of 17 films of heterostacked MoS$_2$ /WS$_2$ on GaN. (d) Raman spectroscopy of pure MoS$_2$ and WS$_2$ (top) and heterostacks of the materials (bottom) on GaN grown on silicon confirms that the layers are not mixed.

5.3 Characterization of WS$_2$/MoS$_2$ Vertical Heterostacks

Raman Spectroscopy

Raman spectroscopy was carried out for 9, 12, and 16 films of heterostacked MoS$_2$ /WS$_2$ as well as pure MoS$_2$ and WS$_2$ films of similar thickness. Raman peaks are observed at 352 cm^{-1} and 420 cm^{-1} for WS$_2$ and at 383 cm^{-1} and 408 cm^{-1} for MoS$_2$, which are the E$^1_{2g}$ (in-plane) and A$_{1g}$ (out-of-plane) modes, respectively. Raman peaks of the heterostacked films resemble the MoS$_2$ and WS$_2$ Raman peaks, indicating that MoS$_2$ and WS$_2$ are grown layer by layer and not mixed.[84,85] The intensity of both E$^1_{2g}$ and A$_{1g}$ modes increases as the thickness increases. The main peak at 520 nm originates from the silicon substrate.

Photoluminescence (PL)

We characterized the photoluminescence as a function of film number at room temperature: Figure 5.3a shows how the PL intensity increases with film number; each film contains 2-3 layers of the respective material. Thus, a 9-film heterostack has approximately 20 TMD layers composed of alternating bilayers of the two materials, with a slightly thicker initialization film. At a film number below 6, we do not observe significant photoluminescence; neither do films of pure MoS_2 or WS_2 exhibit PL on GaN, irrespective of layer number. The PL peak is centered around ~1.9 eV for all films, close to the native MoS_2 PL feature at 1.87 eV.[46,55] We do not observe significant intensity in the trion peaks or B exciton.

We optimized the growth temperature of our substrates to optimize PL intensity. Figure 5.3b shows how the PL yield increases with growth temperature; we attribute this to higher uniformity and lower defect density in our films. The highest intensity is found for a substrate temperature of 710 °C during growth. Further increase of the growth temperature leads to reduced PL intensity, presumably due to increased intermixing of the transition metals. Figure 5.2 shows photographs of the samples obtained at different growth temperatures.

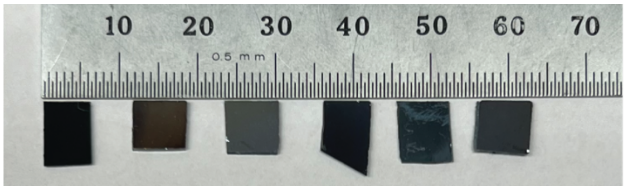

Figure 5.2 Photo of 17 films stack grown at different temperatures on GaN from left to right: 680 °C, 710 °C, 740 °C, 770 °C, 800 °C, 830 °C.

As we cool the sample during PL measurements [Figure 5.3c], we find a blue shift that is well-known in literature and is attributed to the thermal contraction of the material.[86,87] The peak shape remains largely unchanged and no new features emerge even as cold as 5K attesting to the homogeneity of the material. Fig. S2 shows lateral sampling of the PL signal across the growth substrate.

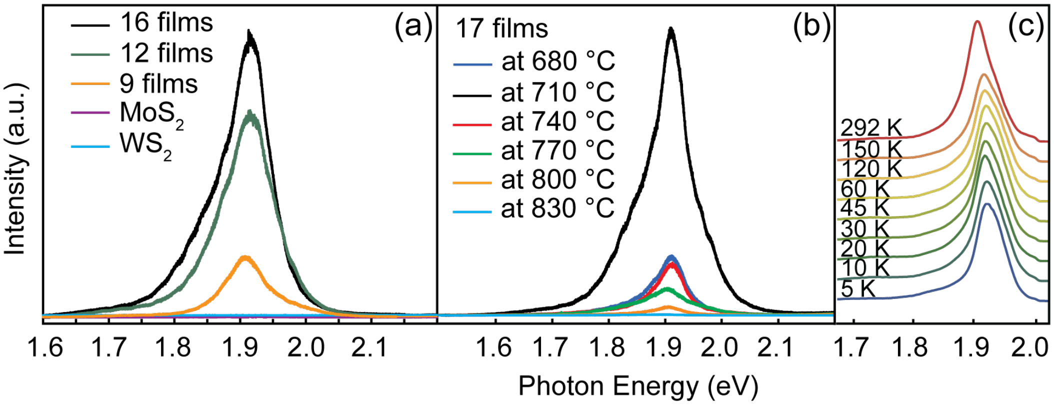

Figure 5.3 (a) PL spectra obtained at Heterostacks of MoS_2/WS_2 (9, 12, and 16 films) and thick films of pure MoS_2 and WS_2 on GaN. (b) PL spectra of 17 films stack grown at different temperature on GaN. (c) PL spectra obtained on a 9 films heterostack at different temperatures from 292K to 5K.

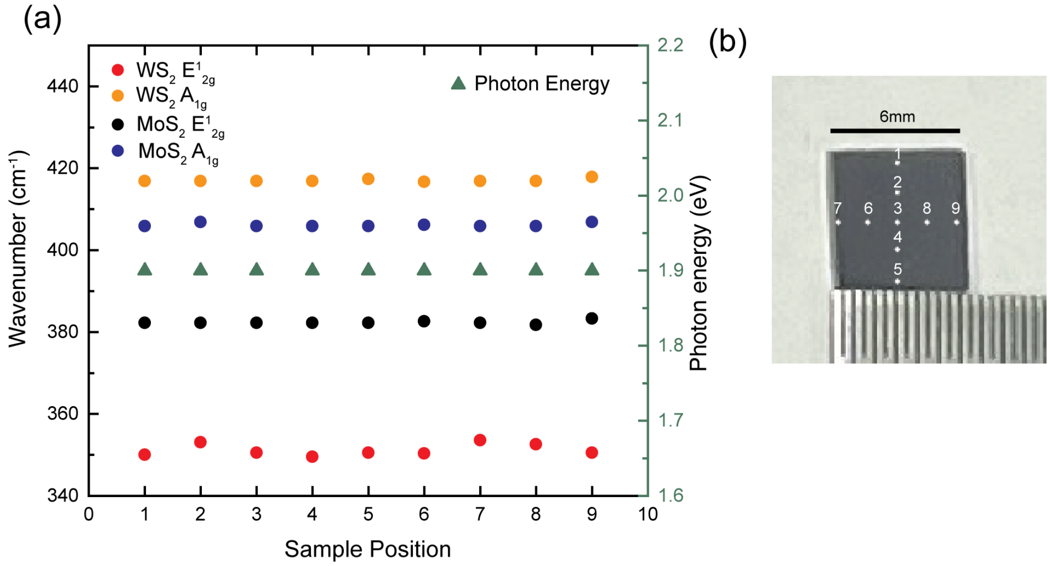

Figure 5.4 Variation of PL and Raman peak positions across the substrate.

Composition and Structure of the Heterostack

To further exclude inhomogeneities in our films as the origin of the PL signal, we obtained cross-sectional transmission electron microscopy (TEM) images resolving the atom columns [Figure 5.5a]. The tungsten- and molybdenum layers are distinct by their electron scattering intensity (bright tungsten, less bright molybdenum), as is confirmed by spatially-resolved energy-dispersive X-ray spectroscopy (EDS) [Figure 5.5b]. A statistical analysis of the atom positions reveals similar layer spacing between the MoS_2 and MoS_2, WS_2 and WS_2, and at the heterolayer interface. Figure 5.5c shows the atom positions of panel a laterally expanded. Here it becomes obvious that the initial MoS_2 film exhibits the A-B stacking typical of 2H MoS_2. As the first tungsten layer is added, the stacking transitions largely to the A-B-C sequence of 3R MoS_2.

We performed density functional theory calculations using the Vienna ab-initio simulation package (VASP).[88,89] We used a 2×2 substrate unit cell to capture the 2×2 reconstruction of the GaN-MoS_2 substrate faithfully.[26] Using 12 layers of GaN and 10 layers of MoS_2/WS_2, we compare in each case the energy of a system stacked in the 2H fashion throughout the TMD layer to that of a system stacked in 3R for the top 6 TMD layers [Figure 5.5e]. In the case of MoS_2, we find insignificant difference in energy between the two configurations (~ 1meV per layer in a 2×2 unit cell). In contrast, for WS_2 we find a substantial preference for 3R stacking by 250 meV for the 2×2 computational supercell [Figure 5.5f]. We performed the same calculation for a range of GaN lattice parameters to cover both the growth temperature and room temperature. We thus conclude that the presence of tungsten is suitable to convert the native 2H stacking of MoS_2 to 3R. We note that this is also born out by mineralogical experience, where tungsten- and rhenium-rich molybdenite deposits show a higher propensity for 3R stacking.[8,90,91]

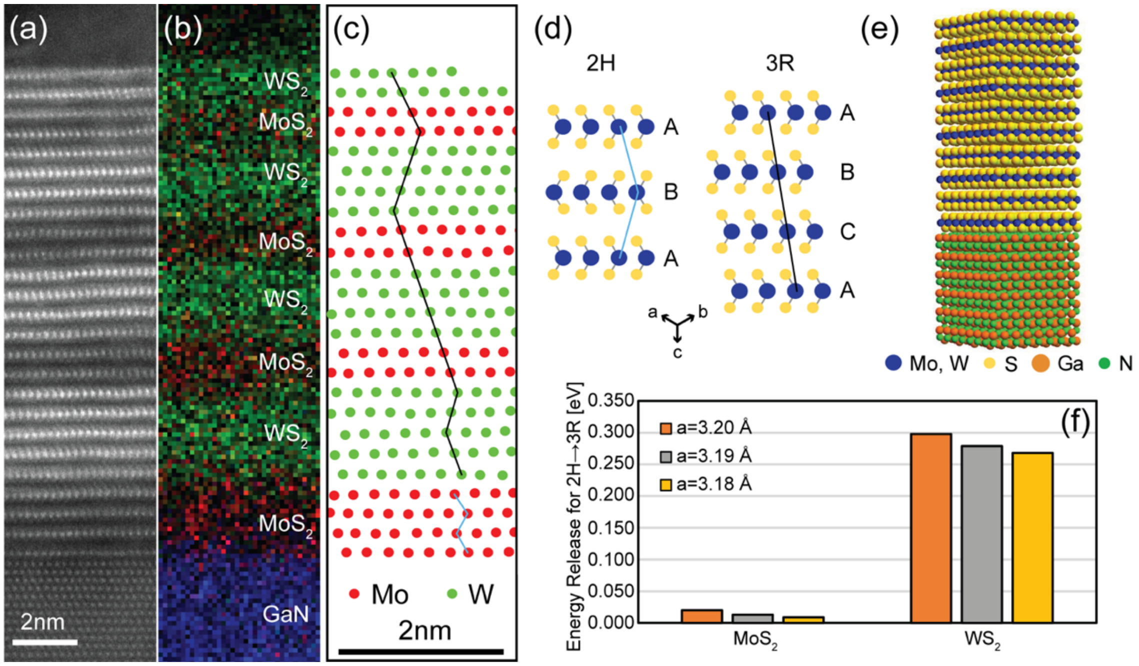

Figure 5.5 (a) Cross-sectional STEM images with EDS (b) of 8 sequences stacked WS_2/MoS_2 layers on GaN, Mo Kα (red), W Lα (green), Ga Kα (navy). (c) Mo and W atom positions in a expanded x-axis. (d) Difference of the 2H and 3R stacking in a sideview. (e) A 2×2 supercell consisting of 12 layers of GaN topped by 10 layers of TMD was used for the computational work. (f) Energy released when the top 6 TMD layers are shifted from the 2H to the 3R configuration.

We note that no (commercial) GaN substrate is perfectly flat on the atomic scale; there are always areas with some growth steps [Figure 5.6]. TEM images of TMD films at growth steps exhibit carpet growth over the steps, leading to strain in the film and internal grain boundaries. As a consequence of the carpet growth, defects are spread out beyond the exact location of the underlying growth step.

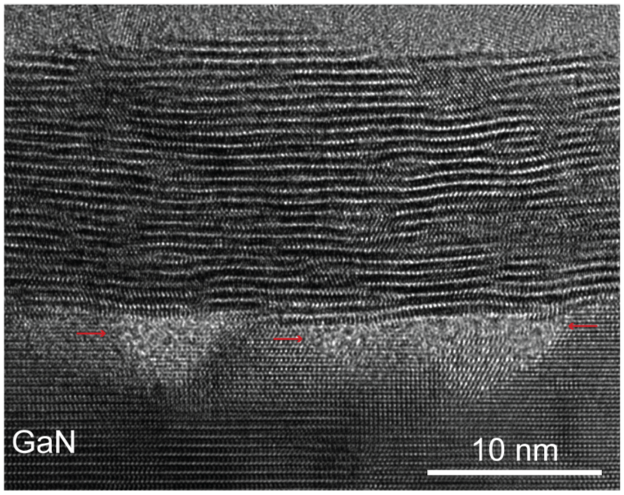

Figure 5.6 TEM image of TMD films on GaN growth steps (annotated by arrows)

To validate epitaxial growth of stacked layers beyond the limited field of view of cross-section TEM, we performed low-energy electron diffraction (LEED), surface characterization technique. We observe a hexagonal diffraction patterns [Figure 5.7a,b]. The absence of rings attests to the pseudo-epitaxial nature of the growth, even for multi-film heterostacks. Figure 5.8 provides further LEED data on films of different thickness.

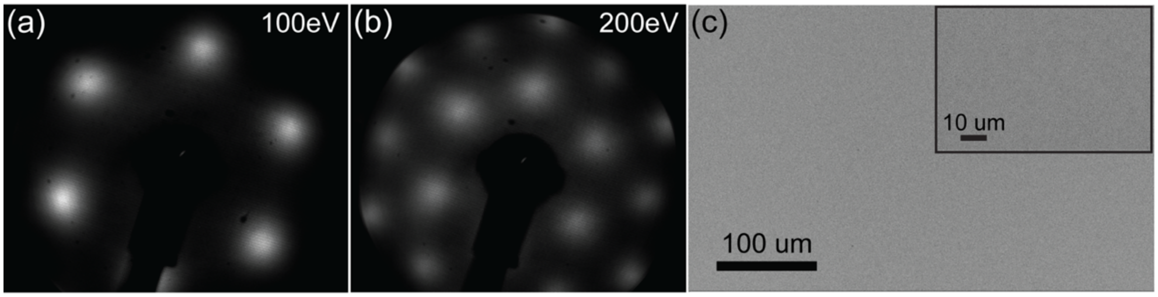

Figure 5.7 (a,b) LEED patterns acquired at a beam energy of 100 eV(left) and 200 eV(right) on a 9 films heterostack. (b) SEM image of 9 films Heterostacks.

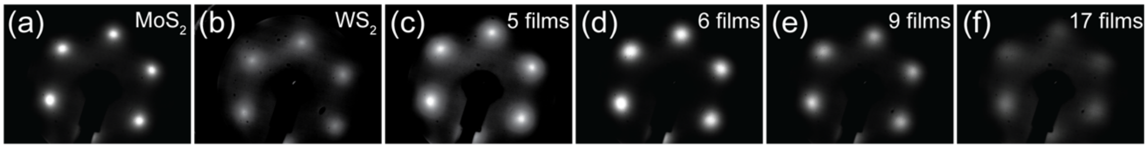

Figure 5.8 LEED patterns at 100eV beam energy for the (a) multilayer MoS_2/GaN, (b) multilayer WS_2/GaN, (c) 5 films heterostack of WS_2/MoS_2 on GaN, (d) 6 films heterostacks of WS_2/MoS_2 on GaN, (e) 9 film heterostacks of WS_2/MoS_2 on GaN, and (f) 17 films heterostacks of WS_2/MoS_2 on GaN.

Figure 5.9a compares the UV-Vis absorption spectra of GaN/sapphire and that of a 12 films heterostack of MoS_2/WS_2 deposited onto the same substrate. The native GaN absorption edge is prominent at 364 nm. The periodic oscillations originate from internal reflection in the sapphire substrate. The heterostack sample shows an additional absorption edge near 500 nm.[92,93,94] For direct analysis, the inset shows the same data plotted as a Tauc plot, in which $(\alpha h\nu)^{1/n}$ is plotted vs. $h\nu$ with h and ν Planck's constant and the frequency of incident light, alpha the absorbance, and n = 2 for direct transitions. This analysis suggests a value of 1.9 eV for the heterostack film and 3.4 eV for GaN.

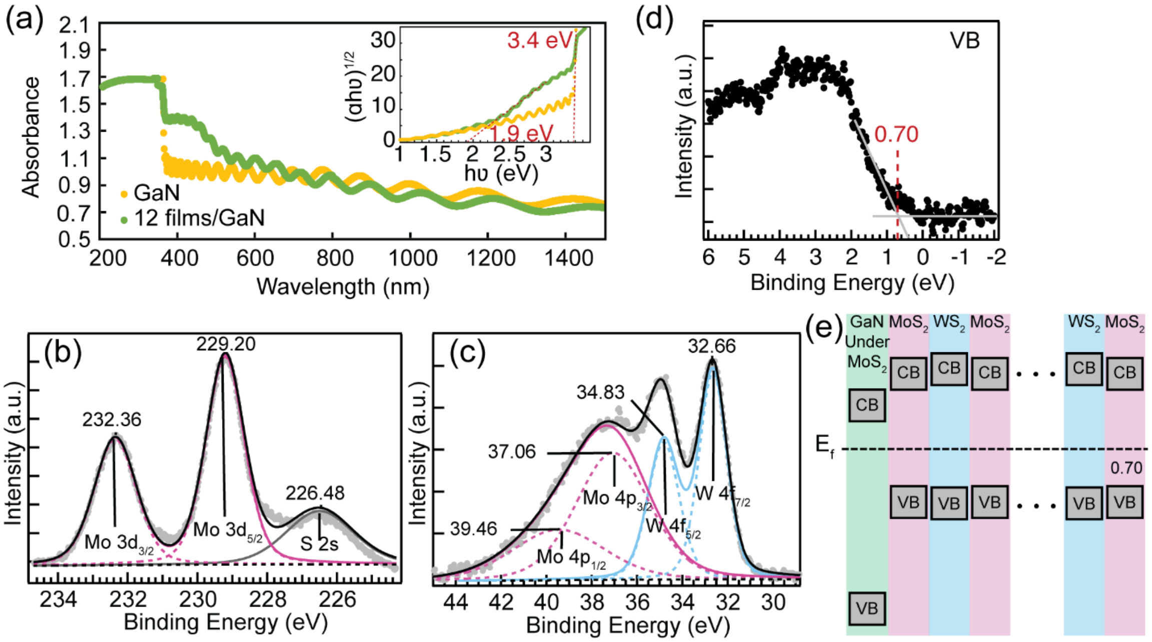

Figure 5.9 (a) UV-Vis absorption spectra of 12 films heterostacks of MoS_2/WS_2 and GaN. The inset shows the Tauc plot. (b) Mo 3d/S 2s (c) W4f/Mo 4p and (d) valence band (VB) edge XPS spectra of 17 films stacks (e) energy band diagram of the VB and conduction band (CB) position of GaN under MoS_2 and heterostacks of MoS_2 and WS_2 based on known band optical gaps of GaN (3.40 eV), WS_2 (2.10 eV), and MoS_2 (1.89 eV)

Electronic Structure

Knowing the optical bandgap of the material, we performed x-ray photoelectron spectroscopy (XPS) to determine the majority charge carrier in this material. We find a valence band (VB) edge of 0.7 eV below the Fermi level [Figure 5.9d] indicating a p-type material similar to single-layer MoS_2/GaN.[71] Analysis of the Mo $4p_{1/2}$ and $4p_{3/2}$, and W $4f_{7/2}$ and W $4f_{5/2}$ core levels [Figure 5.9c] shows the expected [95,96] values for the latter at 32.66 and 34.83 eV, but a set of 37.04 and 39.46 eV for Mo, shifted by 0.1-0.2 eV toward higher binding energy.[97] Likewise, we find the Mo 3d shifted to higher binding energy by about 0.16 eV [Fig. 5.9b].

We interpret this shift as an indicator for accumulation of the hole carriers in the MoS_2 layers. Thus, in the PL experiments, photoexcited electrons in the tungsten layer can reduce their energy by hopping to the adjacent MoS_2 layer. Our observation of bright photoluminescence suggests that at this non-centro-symmetric interface in the 3R stacking a direct transition may be allowed resulting in bright PL. Indeed, literature reports affirm the presence of PL in 3R stacked TMD materials.[98]

Electrical Transport Properties

Finally, we seek to validate continuity of our films by electrical transport measurements. Figure 5.10a shows the device geometry we employ; each pad has a size of 120×120 microns. We fabricate these pads by covering a portion of the sample during growth by means of a tantalum foil. Contact pads to the heterostack side of the film are prepared by electron beam lithography, deposition of a Ti-Au stack, and lift-off. Contacts to the bare GaN are fabricated by means of initial sputtering of the entire wafer piece (the gold-contacts to the heterostack serve as a hardmask) followed by deposition of a Ti-Al-Au stack. The contact pads have a size of 120um and are 40um separated from each other. We perform 3-point measurements applying the source voltage to the inner GaN contact and using the outer GaN contact to sense the voltage drop across the TMD/GaN interface by means of an electrometer. We also confirmed a very low voltage drop (<10 mV) at the contact at the GaN by means of sensing at the outer contact on the GaN side.

Figure 5.10b shows the temperature-dependent IV characteristics of the heterostacks device, which resembles more a Schottky diode with a very low knee voltage than a pn-junction diode. Depending on the temperature, we find an on-off ratio of up to 10^6 between +/- 1V. The reverse current is low and at the limit of the resolution of the Keithley 2400 source meter. Increase of the temperature reduces the resistance of the device by approximately one order of magnitude between 295K to 356K.

We fabricated devices on 2, 8 and 12 films and compared their diode characteristics to that found for a single-layer of MoS_2 on GaN.[71] The total resistance of the diode increases with film number; the on-off ratio improves slightly. The fit to the data of Figure 5.10c utilizes $I = I_s \times e^{\frac{V - I\times R}{n\times V_T}} + \frac{V}{V_p} I_p \left(1 - e^{\frac{V}{V_p}}\right)$. I_S is the scale current, n is the ideality factor, I_p is tunneling current at reverse voltage V_p through the thin diode layer,[99] R is the series resistance of the junction[100] and V_T is the thermal voltage taken as $V_T = kT/q = 25.85$ mV, with k the Boltzmann constant, T the absolute temperature, and q the absolute of the electron charge.

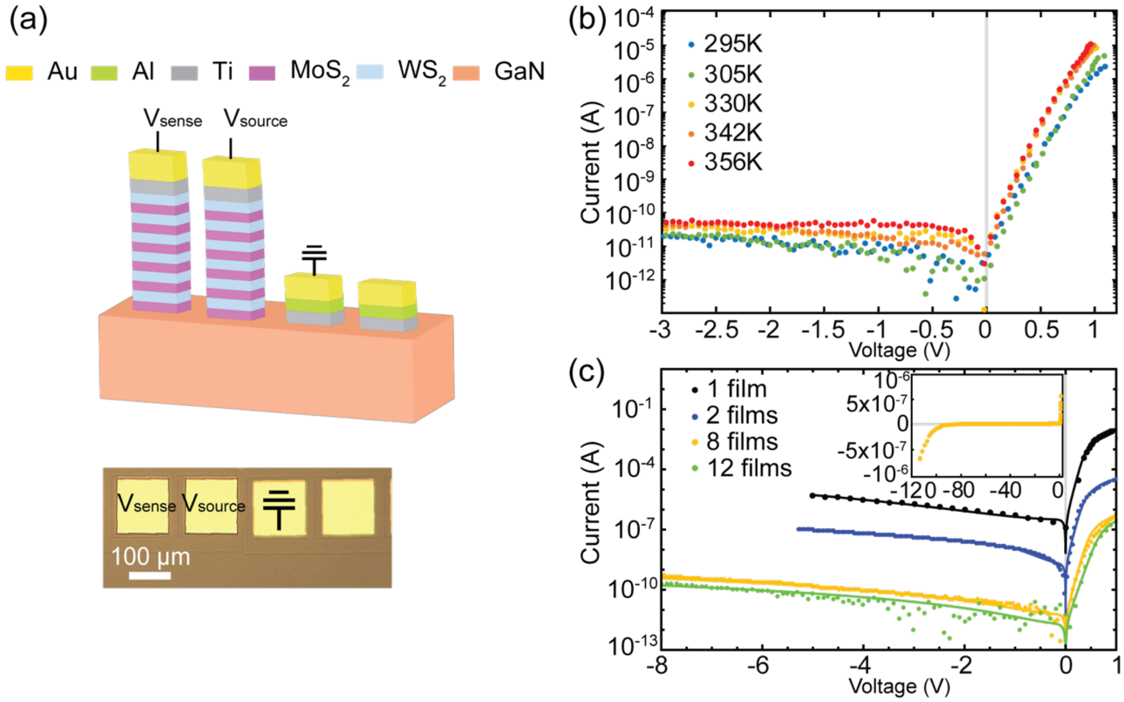

Figure 5.10 (a) Schematic design and an optical image of Heterostacks of MoS$_2$/WS$_2$ device. (b) temperature dependence of current vs. voltage for 8 films Heterostack of MoS$_2$/WS$_2$ device. The inset shows the temperature dependence of current vs. voltage at different bias acquired at 12 films and 8 films of the Heterostack device. (c) I-V characteristics of 1, 2, 8, and 12 films Heterostack MoS$_2$/WS$_2$ device. The inset shows that reverse-voltage breakdown of 8 films Heterostack device is at 100V.

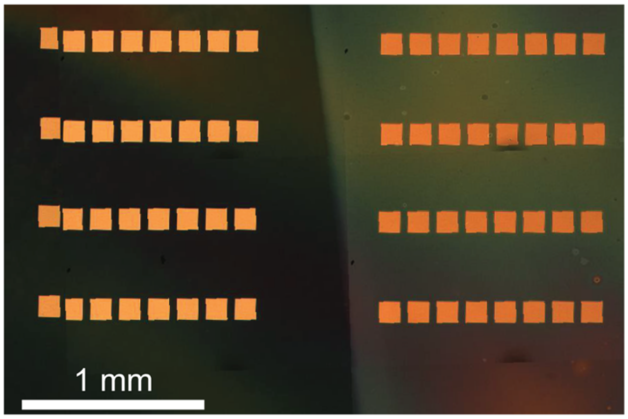

Figure 5.11 Optical image of contacts fabricated on 8 films stack (right side) on GaN (left side).

The quality of the TMD heterostack film is documented by a very large breakthrough voltage >100V for 8 films. This is a substantial value at ~10 nm thickness. Beyond 8 films, we were not able to measure across the breakthrough point without irreversible damage to the film. The high reverse resistance indicates the absence of pinholes or conducting defects in the material. The device performances in this study achieved a higher current on/off ratio and less leakage current density at -1V than the performance reported in the literatures. (Table 5.1)

Materials	**I_{On}/I_{Off} at ±1V**	**Current Density at -1V [A/cm^2]**	**V_{knee} [V]**	**Ideal Factor**	**Breakdown Voltage [V]**	**Ref.**
MoS_2/GaN	$\approx 10^5$	$\approx 4\times10^{-3}$	≈0.3	≈1.8	≈ -20	Our study[48]
8 films Heterostack $MoS_2/WS_2/GaN$	**$\approx 10^7$**	**2.4×10^{-6}**	**≈0.002**	**≈1.9**	**> -100**	**Our study**
12 films Heterostack $MoS_2/WS_2/GaN$	**$\approx 10^6$**	**8.0×10^{-8}**	**≈0.01**	**≈2.4**	**> -100**	**Our study**
MoS_2/GaN	≈1	$\approx 2.2\times10^{-2}$	3.2	1.3	-	101
MoS_2/GaN	≈1	-	-	11	-	102
MoS_2/GaN	$\approx 10^2$	-	-	5.2	-	34
MoS_2/GaN	10	$\approx 10^{-6}$	-	≈1.8	-	103
MoS_2/Si	1	$\approx 10^{-7}$	-	≈3.4	-	103
MoS_2/Ge	≈1	$\approx 2\times10^{-2}$	-	-	-	104
MoS_2/Black Phosphorus	$\approx 10^2$	-	-	≈7	-	105
MoS_2/SiC	$\approx 10^5$	$\approx 10^{-8}$	-	1.25	-	106
MoS_2/SiC	$\approx 10^5$	≈0.3	2.2	2.1		107
WS_2/GaN	$\approx 10^2$	2.96×10^{-5}	0.5	-	-	108
Pt/SiC	$\approx 10^5$	$\approx 10^{-3}$	≈0.6	1.2	-	109
n-GaN/p-GaN	$\approx 10^2$	$\approx 10^{-6}$	≈3	-	-	110

Table 5.1 TMD and 3D semiconductor-based diodes with their device performances

In summary, we have shown that within minutes heterostacks of MoS_2 and WS_2 can be grown on GaN in a pseudo-epitaxial fashion that creates substrate-aligned layers with bright photoluminescence at multilayer thickness. As such, the heterostacks generated here resemble in properties the single layer material, while being substrate-scale homogeneous, pinhole-free at least on the scale of our 120 × 120um contacts, and resilient to lithographic processing.

5.4 WS_2/MoS_2 vs MoS_2/WS_2

The combination of 2D materials with different physical properties and their interaction has been an interest for unique heterojunction configurations such as MoS_2/WS_2,[111,112] MoS_2/WSe_2,[113] $MoSe_2/WSe_2$,[114] WS_2/WSe_2,[115] and applications.[116,85,117] A number of prior studies addressed heterolayer growth on amorphous SiO_2/Si (see table 5.1) However, to our knowledge, no prior epitaxial hetero-layer growth has been reported.

Herein, we introduce the epitaxial growth of 2D materials WS_2/MoS_2 on 3D materials GaN. Then, we discuss the in-depth comparison of WS_2/MoS_2 and WS_2/MoS_2 stacked on GaN. To investigate this research, we developed a high-vacuum-based method that allows us to grow TMD stacks in situ with pristine interfaces at wafer-scale homogeneity without the presence of any powder/particulate precursors or reaction products. We ascertained the epitaxial orientation of the MoS_2/WS_2 layers on GaN throughout the entire TMD stack, as demonstrated by low energy electron diffraction (LEED). To investigate the layer arrangement, we performed transmission electron microscopy (TEM). X-ray photoelectron spectroscopy (XPS) allow us to resolve small shifts in Valence band edge and core levels in each layer, that provides information about interlayer charge transfer.

Papers	Substrate	First Step		Second Step		Extra Step		Characterization
		First Material		Second Material				
MoS_2/WS_2[116]	SiO_2/Si	W 1nm	E-beam evap	Mo 1nm	E-beam evap	Ar^+H_2S plasma, 30-90min, 300°C	Plasma Enhanced CVD	Raman, XPS, TEM, EDS, AFM, UV-Vis, IV curve
WS_2/MoS_2[118]	SiO_2/Si	MoO_3/WO_2, S powders	CVD tube furnace, 200°C	MoO_3/WO_2, S powders	CVD tube furnace, 750°C	-	-	Raman, PL under strain test, TEM
WS_2/MoS_2[85]	SiO_2/Si	Mo 1nm	Magnetron sputtering	W 1nm	Magnetron sputtering	Purge/flush cycles with Ar gas at 750°C →Reaction S power at 300-500°C	CVD tube furnace	Raman, TEM, EDS, AFM, IV curve
Nb-doped WS_2/MoS_2 lateral heterostructure[117]	SiO_2/Si	$(NH_4)_6(H_2W_{12}O_{42}).4H_2O$, Na_2MoO_4, $C_4H_4NNbO_9$	Spin-coated	500°C in air to convert W and Nb into oxide S powder at 200°C→MoS_2 grown at 700°C→Nb-WS_2 lateral grown at 800°C			CVD tube furnace	Raman, PL, XPS, TEM, EDS, AFM, IV curve
WS_2/MoS_2 Vertical and lateral heterostructure[119]	SiO_2/Si	W, Te MoO_3, S powder	CVD tube furnace,850°C	-	-	-	-	Raman, PL, STEM, EDS, AFM
			CVD tube furnace,650°C	-	-	-	-	
MoS_2/WS_2 vertical heterostructure[120]	Sapphire <0001>	WO_3, S powder	CVD furnace, 900°C	MoO_3, S powder	CVD furnace grown on SiO_2/Si and transferred			Low temperature PL, transient absorption spectra

Table 5.2 WS_2/MoS_2 growth on amorphous SiO_2/Si from literatures

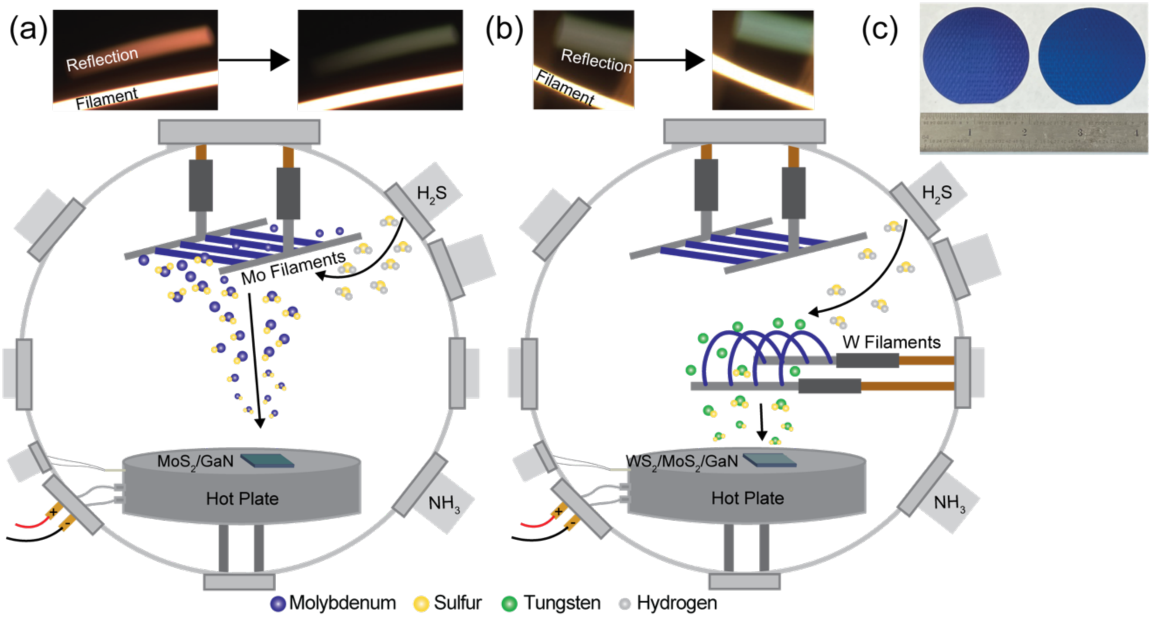

Figure 5.12 Schematic of growth reactors for (a)MoS_2. Hue of the Mo filament and Mo reflection during MoS_2 growth (b) WS_2 and hue of the W filament and W reflection during WS_2 growth (c) photograph of substrates before (300nm SiO_2/Si on the right side) and after WS_2/MoS_2 growth (WS_2/MoS_2/300nm SiO_2/Si on the left side)

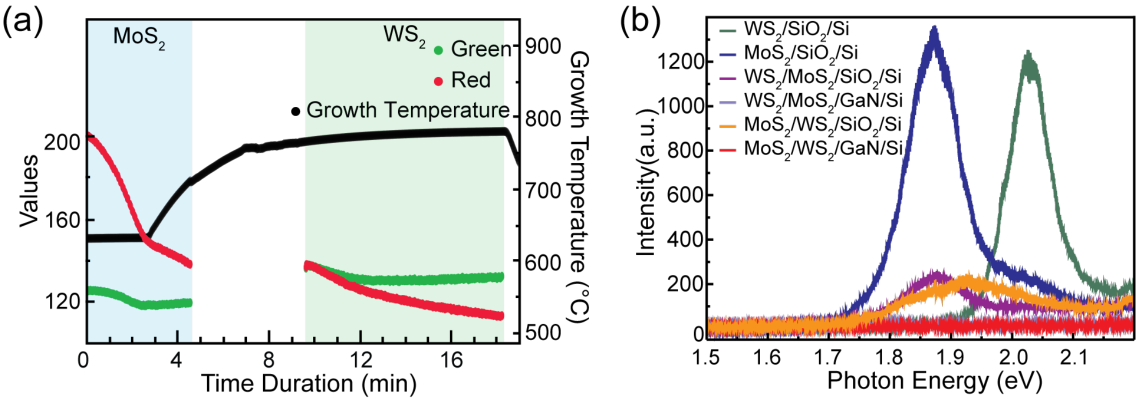

Figure 5.13 (a) Color curves of the filament reflection and temperature profile during growth (b) Photoluminescence of heterostructure and monolayer of MoS_2 and WS_2 on GaN/Si and SiO_2/Si

It is crucial to maintain a clean interface between 2D materials and GaN rather than be disrupted by a dirty interlayer since this affects the device performance of a vertical structure.[24] We elucidated that optimizing the GaN surface treatment achieved low turn-on voltage Schottky-diode behavior of MoS_2/GaN in our past research in Chapter 3. Once the pressure is $1x10^{-7}$ torr, we start sputtering with Neon to remove second-period contaminants using a sputter dose of 30 mC/cm^2. Next, annealing treatment with Ammonia at a hot plate temperature of 750 °C for 15 minutes is performed to achieve a well-defined nitrogen-terminated GaN surface. MoS_2 and WS_2 growth are achieved, as shown in Figure 5.13. GaN is cooled down to a hot plate temperature of 650 °C, and hydrogen sulfide is dosed to 2×10^{-3} torr. At a hot plate temperature of 650 °C, Multilayers MoS_2 are grown using hot molybdenum filaments of 0.5mm (~1700 °C, white color to the eye of a black body thermal radiator).[26,48] The H_2S is decomposed by hot molybdenum and creates MoS_x precursors. The growth process is monitored by recording the reflection of the hot filament from a 300nm SiO_2/Si substrate. Red and Green color components (0-255) are decomposed, which allows us to track filament brightness and film deposition. [Figure 5.13a]. We can control layer thickness precisely while staying on the same filament brightness. Once Red and green component values are crossed during the growth, we finished growth of bilayers of MoS_2 and ramped up the hot plate temperature to 788 °C for WS_2 growth. WS_2 deposition is carried out using hot tungsten filaments of 0.2794 mm (~over 1700 °C). The growth mechanism is the same as MoS_2 deposition. In terms of the reflection, we stopped it once the green component was ~30 above the red one. It takes 5 and 8 min for MoS_2 and WS_2 growth, respectively.

Fig 5.13b shows the photoluminescence (PL) signal as obtained for single-layers of MoS_2 and WS_2 on SiO_2 with well-established peaks at about 1.9 and 2.1 eV. Films grown on GaN do not exhibit any PL, as the exciton dissociates between the overlayer and the GaN bulk.[71] Monolayer stacks of MoS_2/WS_2 and WS_2/MoS_2 type exhibit an MoS_2-like PL signal suggesting near-quantitative non-radiative transfer of the exciton of the lower bandgap material.

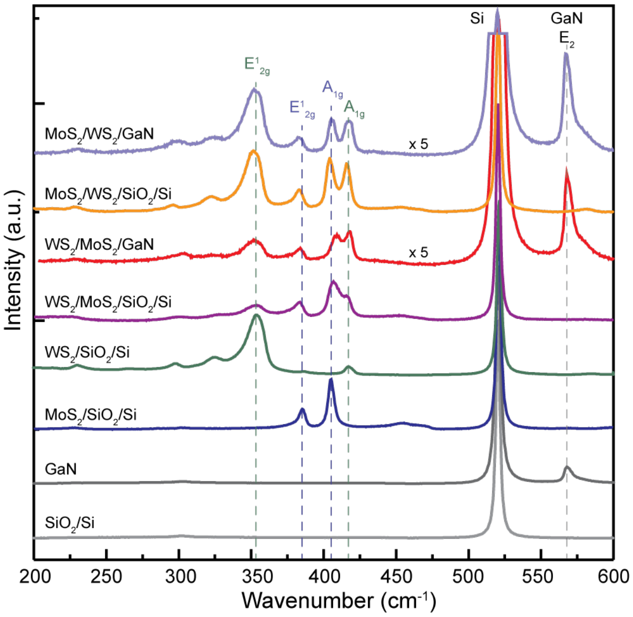

Figure 5.14 Raman spectrum for the heterostructure and individual monolayers of MoS_2 and WS_2 on a different substrate GaN and SiO_2/Si

Raman spectroscopy was carried out for MoS_2 /WS_2 layers and WS_2/MoS_2 on GaN and SiO_2/Si [Figure 5.14]. Raman peaks are observed at 352cm^{-1} and 420cm^{-1} for WS_2 and at 383 cm^{-1} and 408cm^{-1} for MoS_2, which are associated with E^1_{2g} (in-plane vibration) mode and A_{1g} (out-of-plane mode), respectively. Raman peaks of each hetero stacked layer correspond to MoS_2 and WS_2 Raman peaks, indicating that MoS_2 and WS_2 are grown layer by layer and not mixed.[85] The intensity of both E^1_{2g} and A_{1g} modes increases as the thickness increases. Compared with MoS_2, red shift of E^1_{2g} of MoS_2in the MoS_2 /WS_2 layers and WS_2/MoS_2 are observed, suggesting tensile strain of heteorstacks.[118]

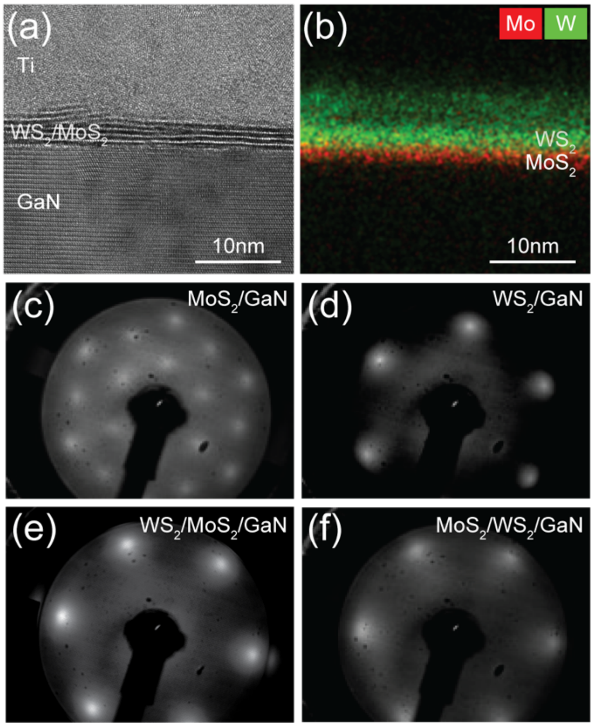

Figure 5.15 (a)cross-sectional scanning TEM image (b) EDS elemental images of WS_2/MoS_2/GaN. LEED patterns obtained at 70 eV beam energy on (c) MoS_2/GaN, (d)WS_2/GaN, (e) WS_2/MoS_2/GaN, (f) MoS_2/WS_2/GaN structure

We performed cross-sectional transmission electron microscopy with EDS elemental resolution [Figure 5.15 a,b]. The result shows a well-layered nature of our film and, within the instrument resolution, no intermixing between the Mo and W layers. To validate epitaxial growth of stacked layers, we performed a low-energy electron diffraction

(LEED) surface characterization technique. We observe the hexagonal diffraction patterns (1×1) in WS_2/GaN, WS_2/MoS_2/GaN, and MoS_2/WS_2/GaN and 2×2 patterns in MoS_2/GaN [Figure 5.15c-f], which reveals that there is no contamination layer between layers as well as good periodicity of WS_2/ MoS_2 layers on the GaN.

Summary

This thesis focused on epitaxial growth mechanisms and the characteristics of heterostructures based on TMDs (MoS_2, WS_2) and GaN under a high vacuum system. By means of materials with similar lattice constants and crystallographic orientation, this study sought to optimize the growth condition with a clean interface and enhance the performance of the MoS_2/GaN device. Via unique synthesis, device fabrication, and characteristics, the following was revealed: (i) atomistic control of the interface and MoS_2 on GaN. (ii) Optimal GaN growth mechanism, (iii) alternating WS_2 and MoS_2 heterostructure with enhanced.

To begin with, thin film MoS_2 on GaN with a sputter gradient is explored so as to validate epitaxial growth and the GaN-MoS_2 interface. With an optimal sputter gradient, the favorable configuration was shown on the N-terminated surface, resulting in a 2×2 superstructure. We found that the optimization of the interface led to high-quality MoS_2/GaN diodes with a high on-off ratio (10^5) and low knee voltage (~0.3V).

Optimal interface preparation gave a pathway to grow GaN so as for GaN/MoS_2/GaN npn heterojunction bipolar transistors. To synthesize and optimize high-quality GaN, we attempted GaN growth on MoS_2 by controlling several parameters. We concluded that the growth of high crystallinity GaN needs a higher temperature and lattice matched WS_2 for freestanding from heat as well as epitaxial growth.

Lastly, alternating MoS_2 and WS_2 layers on GaN are shown to exhibit strong red photoluminescence and epitaxial growth with 3R stacking order. In addition, a high on-off ratio (10^6) and high breakthrough voltage (-100V) were observed in heterostacks. Heterostacks with the persistence of bright PL and decent diode behavior can be further used in applications such as photonic devices.

References

(1) Mak, K. F.; Lee, C.; Hone, J.; Shan, J.; Heinz, T. F. Atomically Thin MoS 2 : A New Direct-Gap Semiconductor. *Phys. Rev. Lett.* **2010**, *105* (13). https://doi.org/10.1103/PhysRevLett.105.136805.

(2) Splendiani, A.; Sun, L.; Zhang, Y.; Li, T.; Kim, J.; Chim, C.-Y.; Galli, G.; Wang, F. Emerging Photoluminescence in Monolayer MoS $_2$. *Nano Lett.* **2010**, *10* (4), 1271–1275. https://doi.org/10.1021/nl903868w.

(3) Radisavljevic, B.; Radenovic, A.; Brivio, J.; Giacometti, V.; Kis, A. Single-Layer MoS2 Transistors. *Nat. Nanotechnol.* **2011**, *6* (3), 147–150. https://doi.org/10.1038/nnano.2010.279.

(4) Wu, R.; Tao, Q.; Dang, W.; Liu, Y.; Li, B.; Li, J.; Zhao, B.; Zhang, Z.; Ma, H.; Sun, G.; Duan, X.; Duan, X. Van Der Waals Epitaxial Growth of Atomically Thin 2D Metals on Dangling-Bond-Free WSe2 and WS2. *Adv. Funct. Mater.* **2019**, *29* (12), 1806611. https://doi.org/10.1002/adfm.201806611.

(5) Eichfeld, S. M.; Hossain, L.; Lin, Y.-C.; Piasecki, A. F.; Kupp, B.; Birdwell, A. G.; Burke, R. A.; Lu, N.; Peng, X.; Li, J.; Azcatl, A.; McDonnell, S.; Wallace, R. M.; Kim, M. J.; Mayer, T. S.; Redwing, J. M.; Robinson, J. A. Highly Scalable, Atomically Thin WSe2 Grown via Metal–Organic Chemical Vapor Deposition. *ACS Nano* **2015**, *9* (2), 2080–2087. https://doi.org/10.1021/nn5073286.

(6) Tan, L. K.; Liu, B.; Teng, J. H.; Guo, S.; Low, H. Y.; Loh, K. P. Atomic Layer Deposition of a MoS2 Film. *Nanoscale* **2014**, *6* (18), 10584–10588. https://doi.org/10.1039/C4NR02451F.

(7) Yang, H. I.; Park, S.; Choi, W. Modification of the Optoelectronic Properties of Two-Dimensional MoS2 Crystals by Ultraviolet-Ozone Treatment. *Appl. Surf. Sci.* **2018**, *443*, 91–96.

(8) Strachan, J.; Masters, A. F.; Maschmeyer, T. 3R-MoS_2 in Review: History, Status, and Outlook. *ACS Appl. Energy Mater.* **2021**, *4* (8), 7405–7418. https://doi.org/10.1021/acsaem.1c00638.

(9) *High-brightness InGaN/AlGaN double-heterostructure blue-green-light-emitting diodes: Journal of Applied Physics: Vol 76, No 12*. https://aip.scitation.org/doi/abs/10.1063/1.357872 (accessed 2021-05-31).

(10) Nakamura, S.; Mukai, T.; Senoh, M. High-Power GaN P-N Junction Blue-Light-Emitting Diodes. *Jpn. J. Appl. Phys.* **1991**, *30* (Part 2, No. 12A), L1998–L2001. https://doi.org/10.1143/JJAP.30.L1998.

(11) Chowdhury, S.; Swenson, B. L.; Wong, M. H.; Mishra, U. K. Current Status and Scope of Gallium Nitride-Based Vertical Transistors for High-Power Electronics Application. *Semicond. Sci. Technol.* **2013**, *28* (7), 074014. https://doi.org/10.1088/0268-1242/28/7/074014.

(12) Roccaforte, F.; Leszczynski, M. Introduction to Gallium Nitride Properties and Applications. In *Nitride Semiconductor Technology*; Roccaforte, F., Leszczynski, M., Eds.; Wiley, 2020; pp 1–39. https://doi.org/10.1002/9783527825264.ch1.

(13) Ohring, M. The Materials Science of Thin Films.

(14) Pei, J.; Yang, J.; Yildirim, T.; Zhang, H.; Lu, Y. Many-Body Complexes in 2D Semiconductors. *Adv. Mater.* **2019**, *31* (2), 1706945. https://doi.org/10.1002/adma.201706945.

(15) Villaos, R. A. B.; Crisostomo, C. P.; Huang, Z.-Q.; Huang, S.-M.; Padama, A. A. B.; Albao, M. A.; Lin, H.; Chuang, F.-C. Thickness Dependent Electronic Properties of Pt Dichalcogenides. *Npj 2D Mater. Appl.* **2019**, *3* (1), 1–8. https://doi.org/10.1038/s41699-018-0085-z.

(16) Dawson, W. G.; Bullett, D. W. Electronic Structure and Crystallography of $MoTe_2$ and WTe_2. *J. Phys. C Solid State Phys.* **1987**, *20* (36), 6159–6174. https://doi.org/10.1088/0022-3719/20/36/017.

(17) Huang, H. H.; Fan, X.; Singh, D. J.; Chen, H.; Jiang, Q.; Zheng, W. T. Controlling Phase Transition for Single-Layer MTe_2 (M = Mo and W): Modulation of the Potential Barrier under Strain. *Phys. Chem. Chem. Phys.* **2016**, *18* (5), 4086–4094. https://doi.org/10.1039/C5CP06706E.

(18) Laturia, A.; Vandenberghe, W. G. Dielectric Properties of Mono- and Bilayers Determined from First Principles. In *2017 International Conference on Simulation of Semiconductor Processes and Devices (SISPAD)*; 2017; pp 337–340. https://doi.org/10.23919/SISPAD.2017.8085333.

(19) Gupta, P.; Rahman, A. A.; Subramanian, S.; Gupta, S.; Thamizhavel, A.; Orlova, T.; Rouvimov, S.; Vishwanath, S.; Protasenko, V.; Laskar, M. R.; Xing, H. G.; Jena, D.; Bhattacharya, A. Layered Transition Metal Dichalcogenides: Promising near-Lattice-

Matched Substrates for GaN Growth. *Sci. Rep.* **2016**, *6* (1), 23708. https://doi.org/10.1038/srep23708.

(20) Seah, M. P.; Dench, W. A. Quantitative Electron Spectroscopy of Surfaces: A Standard Data Base for Electron Inelastic Mean Free Paths in Solids. *Surf. Interface Anal.* **1979**, *1* (1), 2–11. https://doi.org/10.1002/sia.740010103.

(21) Ertl, G.; Küppers, J. *Low Energy Electrons and Surface Chemistry*; VCH, 1985.

(22) Dumcenco, D.; Ovchinnikov, D.; Marinov, K.; Lazić, P.; Gibertini, M.; Marzari, N.; Sanchez, O. L.; Kung, Y.-C.; Krasnozhon, D.; Chen, M.-W.; Bertolazzi, S.; Gillet, P.; Fontcuberta i Morral, A.; Radenovic, A.; Kis, A. Large-Area Epitaxial Monolayer MoS_2. *ACS Nano* **2015**, *9* (4), 4611–4620. https://doi.org/10.1021/acsnano.5b01281.

(23) Li, W.; Zhang, X.; Meng, R.; Yan, J.; Wang, J.; Li, J.; Wei, T. Epitaxy of III-Nitrides on β-Ga_2O_3 and Its Vertical Structure LEDs. *Micromachines* **2019**, *10* (5), 322. https://doi.org/10.3390/mi10050322.

(24) Ruzmetov, D.; Neupane, M. R.; Herzing, A.; O'Regan, T. P.; Mazzoni, A.; Chin, M. L.; Burke, R. A.; Crowne, F. J.; Birdwell, A. G.; Taylor, D. E.; Kolmakov, A.; Zhang, K.; Robinson, J. A.; Davydov, A. V.; Ivanov, T. G. Van Der Waals Interfaces in Epitaxial Vertical Metal/2D/3D Semiconductor Heterojunctions of Monolayer MoS_2 and GaN. *2D Mater.* **2018**, *5* (4), 045016. https://doi.org/10.1088/2053-1583/aad1b7.

(25) Islam, Z.; Zhang, K.; Robinson, J.; Haque, A. Quality Enhancement of Low Temperature Metal Organic Chemical Vapor Deposited MoS_2: An Experimental and Computational Investigation. *Nanotechnology* **2019**, *30* (39), 395402. https://doi.org/10.1088/1361-6528/ab2c3a.

(26) Almeida, K.; Wurch, M.; Geremew, A.; Yamaguchi, K.; Empante, T. A.; Valentin, M. D.; Gomez, M.; Berges, A. J.; Stecklein, G.; Rumyantsev, S.; Martinez, J.; Balandin, A. A.; Bartels, L. High-Vacuum Particulate-Free Deposition of Wafer-Scale Mono-, Bi-, and Trilayer Molybdenum Disulfide with Superior Transport Properties. *ACS Appl. Mater. Interfaces* **2018**, *10* (39), 33457–33463. https://doi.org/10.1021/acsami.8b10857.

(27) Somorjai, G. A. *Introduction to Surface Chemistry and Catalysis*; Wiley: New York, 1994.

(28) Roldán, R.; Castellanos-Gomez, A.; Cappelluti, E.; Guinea, F. Strain Engineering in Semiconducting Two-Dimensional Crystals. *J. Phys. Condens. Matter* **2015**, *27* (31), 313201. https://doi.org/10.1088/0953-8984/27/31/313201.

(29) Sung, D.; Min, K.-A.; Hong, S. Investigation of Atomic and Electronic Properties of 2D-MoS_2/3D-GaN Mixed-Dimensional Heterostructures. *Nanotechnology* **2019**, *30* (40), 404002. https://doi.org/10.1088/1361-6528/ab2c16.

(30) Wan, Y.; Xiao, J.; Li, J.; Fang, X.; Zhang, K.; Fu, L.; Li, P.; Song, Z.; Zhang, H.; Wang, Y.; Zhao, M.; Lu, J.; Tang, N.; Ran, G.; Zhang, X.; Ye, Y.; Dai, L. Epitaxial Single-Layer MoS_2 on GaN with Enhanced Valley Helicity. *Adv. Mater.* **2018**, *30* (5), 1703888. https://doi.org/10.1002/adma.201703888.

(31) Ruzmetov, D.; Neupane, M. R.; Herzing, A.; O'Regan, T. P.; Mazzoni, A.; Chin, M. L.; Burke, R. A.; Crowne, F. J.; Birdwell, A. G.; Taylor, D. E.; Kolmakov, A.; Zhang, K.; Robinson, J. A.; Davydov, A. V.; Ivanov, T. G. Van Der Waals Interfaces in

Epitaxial Vertical Metal/2D/3D Semiconductor Heterojunctions of Monolayer MoS_2 and GaN. *2D Mater.* **2018**, *5* (4), 045016. https://doi.org/10.1088/2053-1583/aad1b7.

(32) O'Regan, T. P.; Ruzmetov, D.; Neupane, M. R.; Burke, R. A.; Herzing, A. A.; Zhang, K.; Birdwell, A. G.; Taylor, D. E.; Byrd, E. F. C.; Walck, S. D.; Davydov, A. V.; Robinson, J. A.; Ivanov, T. G. Structural and Electrical Analysis of Epitaxial 2D/3D Vertical Heterojunctions of Monolayer MoS_2 on GaN. *Appl. Phys. Lett.* **2017**, *111* (5), 051602. https://doi.org/10.1063/1.4997188.

(33) Greco, G.; Iucolano, F.; Roccaforte, F. Ohmic Contacts to Gallium Nitride Materials. *Appl. Surf. Sci.* **2016**, *383*, 324–345. https://doi.org/10.1016/j.apsusc.2016.04.016.

(34) Moun, M.; Singh, R. Exploring Conduction Mechanism and Photoresponse in *P*- GaN */n*- MoS $_2$ Heterojunction Diode. *J. Appl. Phys.* **2020**, *127* (13), 135702. https://doi.org/10.1063/1.5143015.

(35) Desai, P.; Todankar, B.; Ranade, A. K.; Kondo, M.; Dewa, T.; Tanemura, M.; Kalita, G. Synthesis of MoS_2 Layers on GaN Using Ammonium Tetrathiomolybdate for Heterojunction Device Applications. *Cryst. Res. Technol.* **2021**, *56* (6), 2000198. https://doi.org/10.1002/crat.202000198.

(36) Zhang, K.; Jariwala, B.; Li, J.; C. Briggs, N.; Wang, B.; Ruzmetov, D.; A. Burke, R.; O. Lerach, J.; G. Ivanov, T.; Haque, M.; M. Feenstra, R.; A. Robinson, J. Large Scale 2D/3D Hybrids Based on Gallium Nitride and Transition Metal Dichalcogenides. *Nanoscale* **2018**, *10* (1), 336–341. https://doi.org/10.1039/C7NR07586C.

(37) Lee, J.; Jang, H.; Kwak, T.; Choi, U.; So, B.; Nam, O. Growth and Characterization of MoS2/n-GaN and MoS2/p-GaN Vertical Heterostructure with Wafer Scale

Homogeneity. *Solid-State Electron.* **2020**, *165*, 107751. https://doi.org/10.1016/j.sse.2019.107751.

(38) Krishnamoorthy, S.; Lee, E. W.; Lee, C. H.; Zhang, Y.; McCulloch, W. D.; Johnson, J. M.; Hwang, J.; Wu, Y.; Rajan, S. High Current Density 2D/3D MoS_2 /GaN Esaki Tunnel Diodes. *Appl. Phys. Lett.* **2016**, *109* (18), 183505. https://doi.org/10.1063/1.4966283.

(39) Durmuş, H.; Atav, Ü. Extraction of Voltage-Dependent Series Resistance from I-V Characteristics of Schottky Diodes. *Appl. Phys. Lett.* **2011**, *99* (9), 093505. https://doi.org/10.1063/1.3633116.

(40) Kriplani, N. M.; Bowyer, S.; Huckaby, J.; Steer, M. B. Modelling of an Esaki Tunnel Diode in a Circuit Simulator. *Act. Passive Electron. Compon.* **2011**, *2011*, e830182. https://doi.org/10.1155/2011/830182.

(41) Merida, C. S.; Le, D.; Echeverria, E. M.; Nguyen, A. E.; Rawal, T. B.; Naghibi Alvillar, S.; Kandyba, V.; Al-Mahboob, A.; Losovyj, Y.; Katsiev, K.; Valentin, M. D.; Huang, C.-Y.; Gomez, M. J.; Lu, I.-H.; Guan, A.; Barinov, A.; Rahman, T. S.; Dowben, P. A.; Bartels, L. Gold Dispersion and Activation on the Basal Plane of Single-Layer MoS_2. *J. Phys. Chem. C* **2018**, *122* (1), 267–273. https://doi.org/10.1021/acs.jpcc.7b07632.

(42) Tahersima, M. H.; Birowosuto, M. D.; Ma, Z.; Coley, W. C.; Valentin, M. D.; Naghibi Alvillar, S.; Lu, I.-H.; Zhou, Y.; Sarpkaya, I.; Martinez, A.; Liao, I.; Davis, B. N.; Martinez, J.; Martinez-Ta, D.; Guan, A.; Nguyen, A. E.; Liu, K.; Soci, C.; Reed, E.; Bartels, L.; Sorger, V. J. Testbeds for Transition Metal Dichalcogenide Photonics:

Efficacy of Light Emission Enhancement in Monomer vs Dimer Nanoscale Antennae. *ACS Photonics* **2017**, *4* (7), 1713–1721. https://doi.org/10.1021/acsphotonics.7b00208.

(43) Tang, W.; Sanville, E.; Henkelman, G. A Grid-Based Bader Analysis Algorithm without Lattice Bias. *J. Phys. Condens. Matter* **2009**, *21* (8), 084204. https://doi.org/10.1088/0953-8984/21/8/084204.

(44) Laskar, M. R.; Nath, D. N.; Ma, L.; Lee, E. W.; Lee, C. H.; Kent, T.; Yang, Z.; Mishra, R.; Roldan, M. A.; Idrobo, J.-C.; Pantelides, S. T.; Pennycook, S. J.; Myers, R. C.; Wu, Y.; Rajan, S. P-Type Doping of MoS_2 Thin Films Using Nb. *Appl. Phys. Lett.* **2014**, *104* (9), 092104. https://doi.org/10.1063/1.4867197.

(45) Radisavljevic, B.; Radenovic, A.; Brivio, J.; Giacometti, V.; Kis, A. Single-Layer MoS 2 Transistors. *Nat. Nanotechnol.* **2011**, *6* (3), 147–150. https://doi.org/10.1038/nnano.2010.279.

(46) Mak, K. F.; Lee, C.; Hone, J.; Shan, J.; Heinz, T. F. Atomically Thin MoS_2: A New Direct-Gap Semiconductor. *Phys. Rev. Lett.* **2010**, *105* (13), 136805. https://doi.org/10.1103/PhysRevLett.105.136805.

(47) *Transport in Complex Crystalline Materials Based on van der Waals Heterostructures*. https://apps.dtic.mil/sti/citations/AD1078381 (accessed 2021-11-12).

(48) Yang, H. I.; Coyle, D. J.; Wurch, M.; Yadav, P. R.; Valentin, M. D.; Neupane, M. R.; Almeida, K.; Bartels, L. Epitaxial Molybdenum Disulfide/Gallium Nitride Junctions: Low-Knee-Voltage Schottky-Diode Behavior at Optimized Interfaces. *ACS Appl.*

Mater. Interfaces **2021**, *13* (29), 35105–35112. https://doi.org/10.1021/acsami.1c07306.

(49) Yamada, A.; Ho, K. P.; Maruyama, T.; Akimoto, K. Molecular Beam Epitaxy of GaN on a Substrate of MoS 2 Layered Compound. *Appl. Phys. Mater. Sci. Process.* **1999**, *69* (1), 89–92. https://doi.org/10.1007/s003390050976.

(50) Song, Y.; He, Y.; Li, Y.; Wei, H.; Qiu, P.; Huang, Q.; He, Z.; Die, J.; Peng, M.; Zheng, X. Exploration of Monolayer MoS $_2$ Template-Induced Growth of GaN Thin Films via Plasma-Enhanced Atomic Layer Deposition. *Cryst. Growth Des.* **2021**, *21* (3), 1778–1785. https://doi.org/10.1021/acs.cgd.0c01650.

(51) Lee, C. H.; Zhang, Y.; Johnson, J. M.; Koltun, R.; Gambin, V.; Jamison, J. S.; Myers, R. C.; Hwang, J.; Rajan, S. Molecular Beam Epitaxy of GaN on 2H–MoS2. *Appl. Phys. Lett.* **2020**, *117* (12), 123102. https://doi.org/10.1063/5.0012682.

(52) Powell, R. C.; Lee, N. -E.; Greene, J. E. Growth of GaN(0001)1×1 on Al_2O_3(0001) by Gas-source Molecular Beam Epitaxy. *Appl. Phys. Lett.* **1992**, *60* (20), 2505–2507. https://doi.org/10.1063/1.106948.

(53) Baranov, P. G.; Mokhov, E. N.; Ostroumov, A. O.; Ramm, M. G.; Ramm, M. S.; Ratnikov, V. V.; Roenkov, A. D.; Vodakov, Y. A.; Wolfson, A. A.; Saparin, G. V.; Karpov, S. Y.; Zimina, D. V.; Makarov, Y. N.; Juergensen, H. Current Status of GaN Crystal Growth by Sublimation Sandwich Technique. *Mater. Res. Soc. Internet J. Nitride Semicond. Res.* **1998**, *3*, e50. https://doi.org/10.1557/S1092578300001228.

(54) Moldovan, G.; Roe, M. J.; Harrison, I.; Kappers, M.; Humphreys, C. J.; Brown, P. D. Effects of KOH Etching on the Properties of Ga-Polar n-GaN Surfaces. *Philos. Mag.* **2006**, *86* (16), 2315–2327. https://doi.org/10.1080/14786430500522628.

(55) Splendiani, A.; Sun, L.; Zhang, Y.; Li, T.; Kim, J.; Chim, C.-Y.; Galli, G.; Wang, F. Emerging Photoluminescence in Monolayer MoS_2. *Nano Lett.* **2010**, *10* (4), 1271–1275. https://doi.org/10.1021/nl903868w.

(56) Kim, D.; Pandey, J.; Jeong, J.; Cho, W.; Lee, S.; Cho, S.; Yang, H. Phase Engineering of 2D Materials. *Chem. Rev.* **2023**. https://doi.org/10.1021/acs.chemrev.3c00132.

(57) Guo, H.-W.; Hu, Z.; Liu, Z.-B.; Tian, J.-G. Stacking of 2D Materials. *Adv. Funct. Mater.* **2021**, *31* (4), 2007810. https://doi.org/10.1002/adfm.202007810.

(58) Cheiwchanchamnangij, T.; Lambrecht, W. R. L. Quasiparticle Band Structure Calculation of Monolayer, Bilayer, and Bulk MoS_2. *Phys. Rev. B* **2012**, *85* (20), 205302. https://doi.org/10.1103/PhysRevB.85.205302.

(59) Din, N. U.; Turkowski, V.; Rahman, T. S. Ultrafast Charge Dynamics and Photoluminescence in Bilayer MoS_2. *2D Mater.* **2021**, *8* (2), 025018. https://doi.org/10.1088/2053-1583/abd6b5.

(60) Qiu, D. Y.; Da Jornada, F. H.; Louie, S. G. Erratum: Optical Spectrum of MoS_2: Many-Body Effects and Diversity of Exciton States. *Phys. Rev. Lett.* **2015**, *115* (11), 119901. https://doi.org/10.1103/PhysRevLett.115.119901.

(61) Sarkar, S.; Mathew, S.; Chintalapati, S.; Rath, A.; Panahandeh-Fard, M.; Saha, S.; Goswami, S.; Tan, S. J. R.; Loh, K. P.; Scott, M.; Venkatesan, T. Direct Bandgap-

like Strong Photoluminescence from Twisted Multilayer MoS_2 Grown on $SrTiO_3$. *ACS Nano* **2020**, *14* (12), 16761–16769. https://doi.org/10.1021/acsnano.0c04801.

(62) Eda, G.; Yamaguchi, H.; Voiry, D.; Fujita, T.; Chen, M.; Chhowalla, M. Photoluminescence from Chemically Exfoliated MoS_2. *Nano Lett.* **2011**, *11* (12), 5111–5116. https://doi.org/10.1021/nl201874w.

(63) Kang, S.; Kim, Y. S.; Jeong, J. H.; Kwon, J.; Kim, J. H.; Jung, Y.; Kim, J. C.; Kim, B.; Bae, S. H.; Huang, P. Y.; Hone, J. C.; Jeong, H. Y.; Park, J.-W.; Lee, C.-H.; Lee, G.-H. Enhanced Photoluminescence of Multiple Two-Dimensional van Der Waals Heterostructures Fabricated by Layer-by-Layer Oxidation of MoS_2. *ACS Appl. Mater. Interfaces* **2021**, *13* (1), 1245–1252. https://doi.org/10.1021/acsami.0c18364.

(64) Xiong, G.; Zhu, H.; Wang, L.; Fan, L.; Zheng, Z.; Li, B.; Zhao, F.; Han, Z. Radiation Damage and Abnormal Photoluminescence Enhancement of Multilayer MoS_2 under Neutron Irradiation. *J. Phys. Condens. Matter* **2021**, *34* (5), 055701. https://doi.org/10.1088/1361-648X/ac31f8.

(65) Dhall, R.; Seyler, K.; Li, Z.; Wickramaratne, D.; Neupane, M. R.; Chatzakis, I.; Kosmowska, E.; Lake, R. K.; Xu, X.; Cronin, S. B. Strong Circularly Polarized Photoluminescence from Multilayer MoS_2 Through Plasma Driven Direct-Gap Transition. *ACS Photonics* **2016**, *3* (3), 310–314. https://doi.org/10.1021/acsphotonics.5b00593.

(66) Joo, P.; Jo, K.; Ahn, G.; Voiry, D.; Jeong, H. Y.; Ryu, S.; Chhowalla, M.; Kim, B.-S. Functional Polyelectrolyte Nanospaced MoS_2 Multilayers for Enhanced

Photoluminescence. *Nano Lett.* **2014**, *14* (11), 6456–6462. https://doi.org/10.1021/nl502883a.

(67) Wu, W.; De, D.; Chang, S.-C.; Wang, Y.; Peng, H.; Bao, J.; Pei, S.-S. High Mobility and High on/off Ratio Field-Effect Transistors Based on Chemical Vapor Deposited Single-Crystal MoS_2 Grains. *Appl. Phys. Lett.* **2013**, *102* (14), 142106. https://doi.org/10.1063/1.4801861.

(68) Mann, J.; Sun, D.; Ma, Q.; Chen, J.-R.; Preciado, E.; Ohta, T.; Diaconescu, B.; Yamaguchi, K.; Tran, T.; Wurch, M.; Magnone, K.; Heinz, T. F.; Kellogg, G. L.; Kawakami, R.; Bartels, L. Facile Growth of Monolayer MoS_2 Film Areas on SiO_2. *Eur. Phys. J. B* **2013**, *86* (5), 226. https://doi.org/10.1140/epjb/e2013-31011-y.

(69) Ruzmetov, D.; Zhang, K.; Stan, G.; Kalanyan, B.; Bhimanapati, G. R.; Eichfeld, S. M.; Burke, R. A.; Shah, P. B.; O'Regan, T. P.; Crowne, F. J.; Birdwell, A. G.; Robinson, J. A.; Davydov, A. V.; Ivanov, T. G. Vertical 2D/3D Semiconductor Heterostructures Based on Epitaxial Molybdenum Disulfide and Gallium Nitride. *ACS Nano* **2016**, *10* (3), 3580–3588. https://doi.org/10.1021/acsnano.5b08008.

(70) Ahn, C.; Lee, J.; Kim, H.-U.; Bark, H.; Jeon, M.; Ryu, G. H.; Lee, Z.; Yeom, G. Y.; Kim, K.; Jung, J.; Kim, Y.; Lee, C.; Kim, T. Low-Temperature Synthesis of Large-Scale Molybdenum Disulfide Thin Films Directly on a Plastic Substrate Using Plasma-Enhanced Chemical Vapor Deposition. *Adv. Mater.* **2015**, *27* (35), 5223–5229. https://doi.org/10.1002/adma.201501678.

(71) Yang, H. I.; Coyle, D. J.; Wurch, M.; Yadav, P. R.; Valentin, M. D.; Neupane, M. R.; Almeida, K.; Bartels, L. Epitaxial Molybdenum Disulfide/Gallium Nitride Junctions:

Low-Knee-Voltage Schottky-Diode Behavior at Optimized Interfaces. *ACS Appl. Mater. Interfaces* **2021**, *13* (29), 35105–35112.

(72) Gupta, P.; Rahman, A. A.; Subramanian, S.; Gupta, S.; Thamizhavel, A.; Orlova, T.; Rouvimov, S.; Vishwanath, S.; Protasenko, V.; Laskar, M. R.; Xing, H. G.; Jena, D.; Bhattacharya, A. Layered Transition Metal Dichalcogenides: Promising near-Lattice-Matched Substrates for GaN Growth. *Sci. Rep.* **2016**, *6* (1), 23708. https://doi.org/10.1038/srep23708.

(73) Schulz, H.; Thiemann, K. H. Crystal Structure Refinement of AlN and GaN. *Solid State Commun.* **1977**, *23* (11), 815–819. https://doi.org/10.1016/0038-1098(77)90959-0.

(74) Ghosh, C.; Singh, M. K.; Parida, S.; Janish, M. T.; Dobley, A.; Dongare, A. M.; Carter, C. B. Phase Evolution and Structural Modulation during in Situ Lithiation of MoS_2, WS_2 and Graphite in TEM. *Sci. Rep.* **2021**, *11* (1), 9014. https://doi.org/10.1038/s41598-021-88395-1.

(75) Dumcenco, D.; Ovchinnikov, D.; Marinov, K.; Lazić, P.; Gibertini, M.; Marzari, N.; Sanchez, O. L.; Kung, Y.-C.; Krasnozhon, D.; Chen, M.-W.; Bertolazzi, S.; Gillet, P.; Fontcuberta i Morral, A.; Radenovic, A.; Kis, A. Large-Area Epitaxial Monolayer MoS_2. *ACS Nano* **2015**, *9* (4), 4611–4620. https://doi.org/10.1021/acsnano.5b01281.

(76) Macha, M.; Goo Ji, H.; Tripathi, M.; Zhao, Y.; Thakur, M.; Zhang, J.; Kis, A.; Radenovic, A. Wafer-Scale MoS_2 with Water-Vapor Assisted Showerhead MOCVD. *Nanoscale Adv.* **2022**, *4* (20), 4391–4401. https://doi.org/10.1039/D2NA00409G.

(77) Lee, Y.-H.; Zhang, X.-Q.; Zhang, W.; Chang, M.-T.; Lin, C.-T.; Chang, K.-D.; Yu, Y.-C.; Wang, J. T.-W.; Chang, C.-S.; Li, L.-J.; Lin, T.-W. Synthesis of Large-Area MoS_2 Atomic Layers with Chemical Vapor Deposition. *Adv. Mater.* **2012**, *24* (17), 2320–2325. https://doi.org/10.1002/adma.201104798.

(78) Jin, G.; Lee, C.-S.; Okello, O. F. N.; Lee, S.-H.; Park, M. Y.; Cha, S.; Seo, S.-Y.; Moon, G.; Min, S. Y.; Yang, D.-H.; Han, C.; Ahn, H.; Lee, J.; Choi, H.; Kim, J.; Choi, S.-Y.; Jo, M.-H. Heteroepitaxial van Der Waals Semiconductor Superlattices. *Nat. Nanotechnol.* **2021**, *16* (10), 1092–1098. https://doi.org/10.1038/s41565-021-00942-z.

(79) Jun Toh, R.; Sofer, Z.; Luxa, J.; Sedmidubský, D.; Pumera, M. 3R Phase of MoS_2 and WS_2 Outperforms the Corresponding 2H Phase for Hydrogen Evolution. *Chem. Commun.* **2017**, *53* (21), 3054–3057. https://doi.org/10.1039/C6CC09952A.

(80) Luxa, J.; Spejchalová, L.; Jakubec, I.; Sofer, Z. MoS_2 Stacking Matters: 3R Polytype Significantly Outperforms 2H MoS_2 for the Hydrogen Evolution Reaction. *Nanoscale* **2021**, *13* (46), 19391–19398. https://doi.org/10.1039/D1NR03284D.

(81) Dong, Y.; Yang, M.-M.; Yoshii, M.; Matsuoka, S.; Kitamura, S.; Hasegawa, T.; Ogawa, N.; Morimoto, T.; Ideue, T.; Iwasa, Y. Giant Bulk Piezophotovoltaic Effect in 3R-MoS_2. *Nat. Nanotechnol.* **2023**, *18* (1), 36–41. https://doi.org/10.1038/s41565-022-01252-8.

(82) Park, J.; Yeu, I. W.; Han, G.; Jang, C.; Kwak, J. Y.; Hwang, C. S.; Choi, J.-H. Optical Control of the Layer Degree of Freedom through Wannier–Stark States in Polar 3R

MoS_2. *J. Phys. Condens. Matter* **2019**, *31* (31), 315502. https://doi.org/10.1088/1361-648X/ab1d0f.

(83) Suzuki, R.; Sakano, M.; Zhang, Y. J.; Akashi, R.; Morikawa, D.; Harasawa, A.; Yaji, K.; Kuroda, K.; Miyamoto, K.; Okuda, T.; Ishizaka, K.; Arita, R.; Iwasa, Y. Valley-Dependent Spin Polarization in Bulk MoS_2 with Broken Inversion Symmetry. *Nat. Nanotechnol.* **2014**, *9* (8), 611–617. https://doi.org/10.1038/nnano.2014.148.

(84) Wang, Z.; Liu, P.; Ito, Y.; Ning, S.; Tan, Y.; Fujita, T.; Hirata, A.; Chen, M. Chemical Vapor Deposition of Monolayer $Mo_{1-x}W_xS_2$ Crystals with Tunable Band Gaps. *Sci. Rep.* **2016**, *6* (1), 21536. https://doi.org/10.1038/srep21536.

(85) Woods, J. M.; Jung, Y.; Xie, Y.; Liu, W.; Liu, Y.; Wang, H.; Cha, J. J. One-Step Synthesis of MoS_2/WS_2 Layered Heterostructures and Catalytic Activity of Defective Transition Metal Dichalcogenide Films. *ACS Nano* **2016**, *10* (2), 2004–2009.

(86) O'Donnell, K. P.; Chen, X. Temperature Dependence of Semiconductor Band Gaps. *Appl. Phys. Lett.* **1991**, *58* (25), 2924–2926. https://doi.org/10.1063/1.104723.

(87) Mann, J.; Ma, Q.; Odenthal, P. M.; Isarraraz, M.; Le, D.; Preciado, E.; Barroso, D.; Yamaguchi, K.; von Son Palacio, G.; Nguyen, A.; Tran, T.; Wurch, M.; Nguyen, A.; Klee, V.; Bobek, S.; Sun, D.; Heinz, Tony. F.; Rahman, T. S.; Kawakami, R.; Bartels, L. 2-Dimensional Transition Metal Dichalcogenides with Tunable Direct Band Gaps: $MoS_{2(1-x)}Se_{2x}$ Monolayers. *Adv. Mater.* **2014**, *26* (9), 1399–1404. https://doi.org/10.1002/adma.201304389.

(88) Kresse, G.; Hafner, J. Ab Initio Molecular Dynamics for Liquid Metals. *Phys. Rev. B* **1993**, *47* (1), 558–561. https://doi.org/10.1103/PhysRevB.47.558.

(89) Kresse, G.; Furthmüller, J. Efficient Iterative Schemes for Ab Initio Total-Energy Calculations Using a Plane-Wave Basis Set. *Phys. Rev. B* **1996**, *54* (16), 11169–11186. https://doi.org/10.1103/PhysRevB.54.11169.

(90) Ciobanu, C. L.; Cook, N. J.; Kelson, C. R.; Guerin, R.; Kalleske, N.; Danyushevsky, L. Trace Element Heterogeneity in Molybdenite Fingerprints Stages of Mineralization. *Chem. Geol.* **2013**, *347*, 175–189. https://doi.org/10.1016/j.chemgeo.2013.03.011.

(91) Newberry, R. J. Polytypism in Molybdenite (I); A Non-Equilibrium Impurity-Induced Phenomenon. *Am. Mineral.* **1979**, *64* (7–8), 758–767.

(92) Dong, N.; Li, Y.; Feng, Y.; Zhang, S.; Zhang, X.; Chang, C.; Fan, J.; Zhang, L.; Wang, J. Optical Limiting and Theoretical Modelling of Layered Transition Metal Dichalcogenide Nanosheets. *Sci. Rep.* **2015**, *5* (1), 14646. https://doi.org/10.1038/srep14646.

(93) Ponomarev, E. A.; Neumann-Spallart, M.; Hodes, G.; Lévy-Clément, C. Electrochemical Deposition of MoS_2 Thin Films by Reduction of Tetrathiomolybdate. *Thin Solid Films* **1996**, *280* (1), 86–89. https://doi.org/10.1016/0040-6090(95)08204-2.

(94) Desai, P.; Ranade, A. K.; Shinde, M.; Todankar, B.; Mahyavanshi, R. D.; Tanemura, M.; Kalita, G. Growth of Uniform MoS2 Layers on Free-Standing GaN Semiconductor for Vertical Heterojunction Device Application. *J. Mater. Sci. Mater. Electron.* **2020**, *31* (3), 2040–2048. https://doi.org/10.1007/s10854-019-02723-w.

(95) Zhang, Y.; Zhang, Y.; Ji, Q.; Ju, J.; Yuan, H.; Shi, J.; Gao, T.; Ma, D.; Liu, M.; Chen, Y.; Song, X.; Hwang, H. Y.; Cui, Y.; Liu, Z. Controlled Growth of High-Quality Monolayer WS_2 Layers on Sapphire and Imaging Its Grain Boundary. *ACS Nano* **2013**, *7* (10), 8963–8971. https://doi.org/10.1021/nn403454e.

(96) Ohuchi, F. S.; Jaegermann, W.; Pettenkofer, C.; Parkinson, B. A. Semiconductor to Metal Transition of WS_2 Induced by K Intercalation in Ultrahigh Vacuum. *Langmuir* **1989**, *5* (2), 439–442. https://doi.org/10.1021/la00086a026.

(97) Ganta, D.; Sinha, S.; Haasch, R. T. 2-D Material Molybdenum Disulfide Analyzed by XPS. *Surf. Sci. Spectra* **2014**, *21* (1), 19–27. https://doi.org/10.1116/11.20140401.

(98) Ci, P.; Chen, Y.; Kang, J.; Suzuki, R.; Choe, H. S.; Suh, J.; Ko, C.; Park, T.; Shen, K.; Iwasa, Y.; Tongay, S.; Ager, J. W. I.; Wang, L.-W.; Wu, J. Quantifying van Der Waals Interactions in Layered Transition Metal Dichalcogenides from Pressure-Enhanced Valence Band Splitting. *Nano Lett.* **2017**, *17* (8), 4982–4988. https://doi.org/10.1021/acs.nanolett.7b02159.

(99) Kriplani, N. M.; Bowyer, S.; Huckaby, J.; Steer, M. B. Modelling of an Esaki Tunnel Diode in a Circuit Simulator. *Act. Passive Electron. Compon.* **2011**, *2011*, e830182. https://doi.org/10.1155/2011/830182.

(100) Durmuş, H.; Atav, Ü. Extraction of Voltage-Dependent Series Resistance from I-V Characteristics of Schottky Diodes. *Appl. Phys. Lett.* **2011**, *99* (9), 093505. https://doi.org/10.1063/1.3633116.

(101) Liu, C.; Huang, H.; Choi, W.; Kim, J.; Jung, K.; Sun, W.; Tansu, N.; Zhou, W.; Kuo, H.; Li, X. Hybrid Integration of N-MoS $_2$ /p-GaN Diodes by Quasi-van Der

Waals Epitaxy. *ACS Appl. Electron. Mater.* **2020**, *2* (2), 419–425. https://doi.org/10.1021/acsaelm.9b00607.

(102) Moun, M.; Kumar, M.; Garg, M.; Pathak, R.; Singh, R. Understanding of MoS_2/GaN Heterojunction Diode and Its Photodetection Properties. *Sci. Rep.* **2018**, *8* (1), 11799. https://doi.org/10.1038/s41598-018-30237-8.

(103) Miao, J.; Liu, X.; Jo, K.; He, K.; Saxena, R.; Song, B.; Zhang, H.; He, J.; Han, M.-G.; Hu, W.; Jariwala, D. Gate-Tunable Semiconductor Heterojunctions from 2D/3D van Der Waals Interfaces. *Nano Lett.* **2020**, *20* (4), 2907–2915. https://doi.org/10.1021/acs.nanolett.0c00741.

(104) Sarkar, D.; Xie, X.; Liu, W.; Cao, W.; Kang, J.; Gong, Y.; Kraemer, S.; Ajayan, P. M.; Banerjee, K. A Subthermionic Tunnel Field-Effect Transistor with an Atomically Thin Channel. *Nature* **2015**, *526* (7571), 91–95. https://doi.org/10.1038/nature15387.

(105) Deng, Y.; Luo, Z.; Conrad, N. J.; Liu, H.; Gong, Y.; Najmaei, S.; Ajayan, P. M.; Lou, J.; Xu, X.; Ye, P. D. Black Phosphorus–Monolayer MoS_2 van Der Waals Heterojunction p–n Diode. *ACS Nano* **2014**, *8* (8), 8292–8299. https://doi.org/10.1021/nn5027388.

(106) Giannazzo, F.; Panasci, S. E.; Schilirò, E.; Fiorenza, P.; Greco, G.; Roccaforte, F.; Cannas, M.; Agnello, S.; Koos, A.; Pécz, B.; Španková, M.; Chromik, Š. Highly Homogeneous 2D/3D Heterojunction Diodes by Pulsed Laser Deposition of MoS_2 on Ion Implantation Doped 4H-SiC. *Adv. Mater. Interfaces* **2023**, *10* (1), 2201502. https://doi.org/10.1002/admi.202201502.

(107) Lee, E. W.; Ma, L.; Nath, D. N.; Lee, C. H.; Arehart, A.; Wu, Y.; Rajan, S. Growth and Electrical Characterization of Two-Dimensional Layered MoS2/SiC Heterojunctions. *Appl. Phys. Lett.* **2014**, *105* (20), 203504. https://doi.org/10.1063/1.4901048.

(108) Yu, Y.; Fong, P. W. K.; Wang, S.; Surya, C. Fabrication of WS_2/GaN p-n Junction by Wafer-Scale WS_2 Thin Film Transfer. *Sci. Rep.* **2016**, *6* (1), 37833. https://doi.org/10.1038/srep37833.

(109) Roccaforte, F.; Greco, G.; Fiorenza, P.; Di Franco, S.; Giannazzo, F.; La Via, F.; Zielinski, M.; Mank, H.; Jokubavicius, V.; Yakimova, R. Towards Vertical Schottky Diodes on Bulk Cubic Silicon Carbide (3C-SiC). *Appl. Surf. Sci.* **2022**, *606*, 154896. https://doi.org/10.1016/j.apsusc.2022.154896.

(110) Shin, J.; Kim, H.; Sundaram, S.; Jeong, J.; Park, B.-I.; Chang, C. S.; Choi, J.; Kim, T.; Saravanapavanantham, M.; Lu, K.; Kim, S.; Suh, J. M.; Kim, K. S.; Song, M.-K.; Liu, Y.; Qiao, K.; Kim, J. H.; Kim, Y.; Kang, J.-H.; Kim, J.; Lee, D.; Lee, J.; Kim, J. S.; Lee, H. E.; Yeon, H.; Kum, H. S.; Bae, S.-H.; Bulovic, V.; Yu, K. J.; Lee, K.; Chung, K.; Hong, Y. J.; Ougazzaden, A.; Kim, J. Vertical Full-Colour Micro-LEDs via 2D Materials-Based Layer Transfer. *Nature* **2023**, *614* (7946), 81–87. https://doi.org/10.1038/s41586-022-05612-1.

(111) Gong, Y.; Lin, J.; Wang, X.; Shi, G.; Lei, S.; Lin, Z.; Zou, X.; Ye, G.; Vajtai, R.; Yakobson, B. I.; Terrones, H.; Terrones, M.; Tay, B. K.; Lou, J.; Pantelides, S. T.; Liu, Z.; Zhou, W.; Ajayan, P. M. Vertical and In-Plane Heterostructures from

WS_2/MoS_2 Monolayers. *Nat. Mater.* **2014**, *13* (12), 1135–1142. https://doi.org/10.1038/nmat4091.

(112) He, C.; Wu, R.; Qi, M.; Huang, Y.; Zhou, Y.; Zhang, S.; Zhao, Q.; Xu, X. Dispersion Property and Evolution of Second Harmonic Generation Pattern in Type-I and Type-II van Der Waals Heterostructures. *ACS Appl. Mater. Interfaces* **2021**, *13* (23), 27334–27342. https://doi.org/10.1021/acsami.1c07441.

(113) Li, M.-Y.; Shi, Y.; Cheng, C.-C.; Lu, L.-S.; Lin, Y.-C.; Tang, H.-L.; Tsai, M.-L.; Chu, C.-W.; Wei, K.-H.; He, J.-H.; Chang, W.-H.; Suenaga, K.; Li, L.-J. Epitaxial Growth of a Monolayer WSe_2-MoS_2 Lateral p-n Junction with an Atomically Sharp Interface. *Science* **2015**, *349* (6247), 524–528. https://doi.org/10.1126/science.aab4097.

(114) He, Y.; Yang, Y.; Zhang, Z.; Gong, Y.; Zhou, W.; Hu, Z.; Ye, G.; Zhang, X.; Bianco, E.; Lei, S.; Jin, Z.; Zou, X.; Yang, Y.; Zhang, Y.; Xie, E.; Lou, J.; Yakobson, B.; Vajtai, R.; Li, B.; Ajayan, P. Strain-Induced Electronic Structure Changes in Stacked van Der Waals Heterostructures. *Nano Lett.* **2016**, *16* (5), 3314–3320. https://doi.org/10.1021/acs.nanolett.6b00932.

(115) Gong, Y.; Lei, S.; Ye, G.; Li, B.; He, Y.; Keyshar, K.; Zhang, X.; Wang, Q.; Lou, J.; Liu, Z.; Vajtai, R.; Zhou, W.; Ajayan, P. M. Two-Step Growth of Two-Dimensional $WSe_2/MoSe_2$ Heterostructures. *Nano Lett.* **2015**, *15* (9), 6135–6141. https://doi.org/10.1021/acs.nanolett.5b02423.

(116) Seok, H.; Megra, Y. T.; Kanade, C. K.; Cho, J.; Kanade, V. K.; Kim, M.; Lee, I.; Yoo, P. J.; Kim, H.-U.; Suk, J. W. Low-Temperature Synthesis of Wafer-Scale MoS_2–

WS_2 Vertical Heterostructures by Single-Step Penetrative Plasma Sulfurization. *ACS Nano* **2021**, *15* (1), 707–718.

(117) Vu, V. T.; Phan, T. L.; Vu, T. T. H.; Park, M. H.; Do, V. D.; Bui, V. Q.; Kim, K.; Lee, Y. H.; Yu, W. J. Synthesis of a Selectively Nb-Doped WS_2–MoS_2 Lateral Heterostructure for a High-Detectivity PN Photodiode. *ACS Nano* **2022**, *16* (8), 12073–12082.

(118) Pak, S.; Lee, J.; Lee, Y.-W.; Jang, A.-R.; Ahn, S.; Ma, K. Y.; Cho, Y.; Hong, J.; Lee, S.; Jeong, H. Y. Strain-Mediated Interlayer Coupling Effects on the Excitonic Behaviors in an Epitaxially Grown MoS_2/WS_2 van Der Waals Heterobilayer. *Nano Lett.* **2017**, *17* (9), 5634–5640.

(119) Gong, Y.; Lin, J.; Wang, X.; Shi, G.; Lei, S.; Lin, Z.; Zou, X.; Ye, G.; Vajtai, R.; Yakobson, B. I. Vertical and In-Plane Heterostructures from WS_2/MoS_2 Monolayers. *Nat. Mater.* **2014**, *13* (12), 1135–1142.

(120) Hong, X.; Kim, J.; Shi, S.-F.; Zhang, Y.; Jin, C.; Sun, Y.; Tongay, S.; Wu, J.; Zhang, Y.; Wang, F. Ultrafast Charge Transfer in Atomically Thin MoS_2/WS_2 Heterostructures. *Nat. Nanotechnol.* **2014**, *9* (9), 682–686. https://doi.org/10.1038/nnano.2014.167.